

Power-Law Wrinkling Turbulence-Flame Interaction Model for
Astrophysical Flames

Aaron P. Jackson – Naval Research Laboratory

D. M. Townsley – The University of Alabama

Alan C. Calder – The State University of New York

Deposited 08/23/2018

Citation of published version:

Jackson, A., Townsley, D., Calder, A. (2014): Power-Law Wrinkling Turbulence-Flame Interaction Model for Astrophysical Flames. *The Astronomical Journal*, 784(2).

<http://dx.doi.org/10.1088/0004-637X/784/2/174>

POWER-LAW WRINKLING TURBULENCE–FLAME INTERACTION MODEL FOR ASTROPHYSICAL FLAMES

AARON P. JACKSON^{1,5}, DEAN M. TOWNSLEY², AND ALAN C. CALDER^{3,4}

¹ Laboratories for Computational Physics & Fluid Dynamics, Naval Research Laboratory, Washington, DC, USA

² Department of Physics & Astronomy, The University of Alabama, Tuscaloosa, AL, USA

³ Department of Physics & Astronomy, The State University of New York - Stony Brook, Stony Brook, NY, USA

⁴ Institute for Advanced Computational Science, The State University of New York - Stony Brook, Stony Brook, NY, USA

Received 2013 July 3; accepted 2014 February 16; published 2014 March 18

ABSTRACT

We extend a model for turbulence–flame interactions (TFI) to consider astrophysical flames with a particular focus on combustion in Type Ia supernovae. The inertial range of the turbulent cascade is nearly always under-resolved in simulations of astrophysical flows, requiring the use of a model in order to quantify the effects of subgrid-scale wrinkling of the flame surface. We provide implementation details to extend a well-tested TFI model to low-Prandtl number flames for use in the compressible hydrodynamics code FLASH. A local, instantaneous measure of the turbulent velocity is calibrated for FLASH and verification tests are performed. Particular care is taken to consider the relation between the subgrid rms turbulent velocity and the turbulent flame speed, especially for high-intensity turbulence where the turbulent flame speed is not expected to scale with the turbulent velocity. Finally, we explore the impact of different TFI models in full-star, three-dimensional simulations of Type Ia supernovae.

Key words: hydrodynamics – nuclear reactions, nucleosynthesis, abundances – supernovae: general – turbulence

Online-only material: color figures

1. INTRODUCTION

Type Ia supernovae (SNe) are bright stellar explosions that are characterized by strong P Cygni features in Si and by a lack of hydrogen in their spectra. It has generally been accepted that these events follow from the thermonuclear incineration of a degenerate stellar core known as a white dwarf (WD) that produces $\sim 0.6 M_{\odot}$ of radioactive ^{56}Ni , the decay of which powers the light curve (see Filippenko 1997; Hillebrandt & Niemeyer 2000; Röpke 2006; Calder et al. 2013, and references therein for an overview), and direct evidence for this paradigm was recently established by observations of SN 2011fe (Nugent et al. 2011; Brown et al. 2012; Bloom et al. 2012). The light curves of SNe Ia have the property that the brightness of an event is correlated with its duration. This “brighter is broader” relation (Phillips 1993) is the basis for light curve calibration that allows use of these events as distance indicators for cosmological studies (see Conley et al. 2011 for a contemporary example).

While there is agreement on the general properties of thermonuclear SN, the progenitors of these events are not definitively known and their determination is the subject of active research. The possible progenitor systems are generally divided into two categories: single-degenerate (SD; Whelan & Iben 1973; Nomoto 1982b; Iben & Tutukov 1984) and double-degenerate (DD; Iben & Tutukov 1984; Webbink 1984; i.e., a binary system composed of either one WD or two). In the SD scenario, a ^{12}C - ^{16}O WD accretes material from a main sequence or red giant companion. Either the WD accretes material from its companion until it approaches the Chandrasekhar mass (M_{ch}) sufficiently heating the core to fuse C and begin the thermonuclear runaway (Nomoto 1982b), in which core convection eventually leads to flame ignition (Woosley et al. 2007a), or a layer of He detonates on the surface of a sub- M_{ch} WD driving a compression wave into the core sufficiently strong to trigger

a second detonation (“double-detonation”; Livne 1990). In the DD scenario, two WDs merge via gravitational radiation within a Hubble time. The less massive WD will be tidally disrupted and accreted onto the primary. As long as the accretion rate is not too high to ignite C at the edge (Saio & Nomoto 1985, 1998, 2004), it is possible for the primary to gain enough mass to approach M_{ch} and explode as an SN Ia via the same explosion mechanism as the M_{ch} -WD in the SD channel (Yoon et al. 2007). More recent studies, however, modeling the accretion of an alpha disk driven by the magnetorotational instability find significantly higher accretion rates (Schwab et al. 2012; Ji et al. 2013). Additionally, Pakmor et al. (2010, 2011) recently showed that under certain conditions, the merger is violent enough such that C ignition at the edge may launch a detonation into the primary WD leading to an SN Ia with the brightness primarily determined by the mass of the primary. More recent studies by Dan et al. (2011, 2012), Raskin et al. (2012) find rather different ranges of system masses for successful “violent” detonations.

Chandrasekhar-mass progenitor models have been widely studied as a possible origin of SNe Ia, although the debate between the SD versus DD channel is still very active. One-dimensional delayed detonation models have successfully reproduced many observed features that agree with “normal” SNe Ia (Höflich & Khokhlov 1996). Chandrasekhar mass detonation-only models have been ruled out due to the over-production of ^{56}Ni (Nomoto 1982a; Nomoto et al. 1984) and deflagration-only models cannot account for brighter SNe Ia (Röpke et al. 2007). A delayed detonation mechanism best agrees with many observations of multi-band light curve shapes, nucleosynthetic yields, spectral evolution, and SN remnants (Höflich & Khokhlov 1996; Badenes et al. 2003; Kasen 2006; Kasen & Woosley 2007; Woosley et al. 2007b). This mechanism implies a phase of subsonic burning in which the star may respond to thermonuclear burning and expand before a detonation, or supersonic reaction wave, is somehow initiated to burn any remaining fuel on timescales much shorter than the

⁵ National Research Council Research Associateship Program.

dynamical timescale of the explosion. The standard delayed-detonation model is the so-called deflagration-to-detonation transition (DDT) scenario (Khokhlov 1991) and variations on the DDT scenario, including pulsational detonations (Arnett & Livne 1994a, 1994b; Höflich & Khokhlov 1996; Bravo & García-Senz 2006), gravitationally-confined detonation (Plewa et al. 2004; Jordan et al. 2008) (see also Seitzzahl et al. 2009; Chamulak et al. 2012; Jordan et al. 2012a), and a host of models in which a deflagration transitions to a detonation when the right local conditions are met (Blinnikov & Khokhlov 1986; Woosley 1990; Höflich et al. 1995; Höflich & Khokhlov 1996; Khokhlov et al. 1997; Niemeyer & Woosley 1997; Höflich et al. 1998; Niemeyer 1999) have also been explored.

Thermonuclear flames for compositions, densities, and temperatures characteristic of the C-O WD near conditions for explosive C-burning are spatially thin owing to the extreme temperature dependence of the driving reaction, $^{12}\text{C} + ^{12}\text{C}$ (Timmes & Woosley 1992). A common computational challenge in modeling astrophysical explosions is that typically the physics of combustion is characterized on length scales well below that accessible in simulations that resolve the macroscopic explosive event. In the context of SNe Ia, combustion initially proceeds subsonically, driven by the nuclear fusion of carbon. The flame width of a laminar carbon flame at the densities relevant in the WD is $\lesssim 10^{-1}$ cm, while the WD diameter is $\sim 10^8$ cm. The range of length scales involved in the calculation necessitates the use of a model flame that is resolvable by the computational domain.

Within the standard Chandrasekhar-mass models of SNe Ia, the rising temperature in the core allows carbon fusion before collapse. However, the energy generated from carbon fusion is carried away by convection and a thermonuclear flame is not born for yet another $\sim 10^3$ yr. By the time the energy generation rate exceeds the combined cooling rate from convection and free-streaming neutrinos, the convective region within the core of the WD encompasses $\sim 0.8\text{--}1.0 M_{\odot}$ with a root-mean-squared velocity $v_{\text{rms}} \sim 300 \text{ km s}^{-1}$ (Zingale et al. 2009). While the character of this flow is still the subject of active research, this v_{rms} is higher than the propagation speed of the deflagration front and therefore the turbulence generated by convection is expected to influence the subsequent thermonuclear flame. The magnitude of the effect on the deflagration phase and the subsequent nucleosynthetic yield has not been fully explored in full SN Ia simulations, but the result is that the turbulence-flame interaction (TFI) is essential from the time of first ignition of the deflagration.

The fundamental nature of TFI and, as a result, the best methods to model it in necessarily under-resolved large eddy simulations (LES) is still an outstanding problem in combustion (Driscoll 2008). Thus, there are presently a variety of proposed methods for handling LES TFI that draw on different assumptions and characterizations of the process and rely on different numerical techniques. Due to the prohibitive computational costs involved in validating these assumptions with direct numerical simulation (DNS) for conditions relevant in the SN Ia, one path forward is to address these uncertainties directly by exploring a variety of assumptions for TFI and evaluating the sensitivity to these assumptions. This approach allows effort to be focused on the features of TFI modeling that are most salient to the SN Ia problem. As will be discussed in Section 2.6, the TFI model presented here is intended to complement previous work on TFI in SNe Ia, most notably by Schmidt et al. (2006a, 2006b), by varying some assumptions about the propagation

of turbulence on unresolved scales and some other technical details.

In Section 2, we provide an overview of turbulence and flames, and we briefly discuss differences in current flame modeling approaches. In Section 3 we briefly review the important aspects of the FLASH hydrodynamics code that we use to perform simulations. In Section 4, we describe the implementation details of the method used to measure resolved turbulence following Colin et al. (2000, hereafter CVDP) and calibrate the operator to the FLASH code. In Section 5, we describe the assumptions made to implement a subgrid-scale (SGS) TFI model developed by Charlette et al. (2002a, hereafter CMV) that follows a subgrid flame surface density approach. The TFI model provides a turbulent front propagation speed given the local turbulent intensity and laminar flame properties. In Section 6, we provide simple test problems to verify our scheme behaves as expected. As an aside in Section 7, we provide direction for expanding the model to new regimes of validity in future works. We then compare three different TFI models in full-star, three-dimensional (3D) simulations in Section 8 to highlight differences in model assumptions. We summarize our findings and conclude in Section 9.

2. BACKGROUND ON TURBULENCE AND FLAMES

We begin by outlining some general concepts of turbulence and flames in order to frame our discussion of model flames and TFI. With this introduction and discussion of the important physical length scales and characteristics in the SN, we review briefly what techniques are available and in use to treat flames in simulations of SNe Ia. This discussion motivates the current study by setting out the issues that we hope to address in our numerical models with the TFI presented in this work. Our discussion will focus mainly around techniques used previously in the astrophysical literature and those important to support the methods presented here. For overviews of flame techniques in use in the combustion literature, the reader is referred to Driscoll (2008) and Poinot & Veynante (2005).

2.1. Turbulence

Turbulence occurs in fluid flow under conditions in which the length scales of the flow are significantly greater than the scale of the viscous dissipation of energy, which allows for disordered, stochastic motion and the cascade of energy from large scales to small. Turbulent flows are common in Nature, and influence related phenomena such as mixing and combustion. Turbulence is incompletely understood and research into the nature and properties of turbulent flow continues.

The contemporary understanding of the theory of turbulent flow follows from the work of Kolmogorov (1941, 1991), who introduced the idea of a self-similar cascade of energy from large scales to small. The range between the integral or large driving scale of the flow and the viscous dissipation scale is known as the inertial regime, and depends on the Reynolds number, Re , the ratio of inertial forces to viscous forces, which we may define as $\text{Re} = \ell_t u' / \nu$, where ℓ_t is the integral scale, u' is the turbulent intensity, and ν is the viscosity. A high Reynolds number implies a wide inertial range and turbulent flow. The turbulent intensity measures the relative strength of the turbulence and is defined as $u' \equiv v'_t / \bar{v}$, where v'_t is the root-mean-square of the turbulent velocity fluctuations and \bar{v} is the mean velocity.

The self-similar nature of turbulence in the Kolmogorov model implies that the turbulent flow demonstrates the same

statistical properties on many scales, which allows the description of properties of the turbulent flow via scaling laws. The case of incompressible Kolmogorov turbulence is the famous example of a scaling law (Cho et al. 2003). If v_l is the velocity at scale l within the inertial range, the kinetic energy $\sim v_l^2$ is transferred to the next scale down in one eddy turnover time, $t_{\text{cascade}} = l/v_l$. Kolmogorov theory thus holds that the energy transfer rate is scale-invariant

$$\frac{v_l^2}{t_{\text{cascade}}} = \text{constant}, \quad (1)$$

which yields the Kolmogorov scaling

$$v_l \propto l^{1/3}, \quad (2)$$

which in turn implies the $-5/3$ power law for the power spectrum

$$E(k) \propto k^{-5/3}. \quad (3)$$

Another example of a scaling law we apply below for the case of turbulent combustion is Damköhler scaling, which relates the average flame speed to the turbulence intensity, $s_f \approx u'$.

Experimental and theoretical work, however, indicates that Kolmogorov's theory of turbulence is incomplete because self-similarity is not observed due to the fact that dissipation within the fluid is intermittent in both space and time rather than homogeneous. This situation suggests other scaling laws are necessary for a more accurate description of turbulent flow (See Fisher et al. 2008, for more thorough discussion and an example).

2.2. Flames

We use the term flame or deflagration front to indicate a localized region of exothermic reaction that is propagated into the unreacted material by the diffusion of heat. Assumption of locality means that there exists a well-defined separation between unreacted fuel and fully-reacted products. We note, however, that the diffusion of heat implies a preheating region that extends ahead of the reaction zone, so the assumption of locality applies only to the region of the reaction and not the temperature field. This assumption makes it conceptually similar to a surface that divides space into these two types of regions, though this surface is assumed to have some inherent thickness associated with the detailed mechanism of its reaction and propagation. An important parameter for characterizing astrophysical flames is the Lewis number, $Le = D_{\text{th}}/D_s$ where D_{th} is the thermal diffusivity and D_s is the material diffusivity. In the case of astrophysical flames, the Lewis number is asymptotically large, i.e., thermal diffusion dominates over species diffusion.

2.3. Length Scales

Discussion of turbulence, flames, and TFI necessitates discussion of the length scales of the problem in question, which we briefly outline here. This overview describes the length scales of physics and physical effects that are most relevant to our approach to the problem of premixed flames and TFI in SN Ia explosions and is therefore incomplete. Figure 1 illustrates how the flame might be wrinkled by shear on various scales, and how this is related to some physical and computational scales in our problem. The diagram at the top of Figure 1 demonstrates the two principal competing wrinkling mechanisms that will be

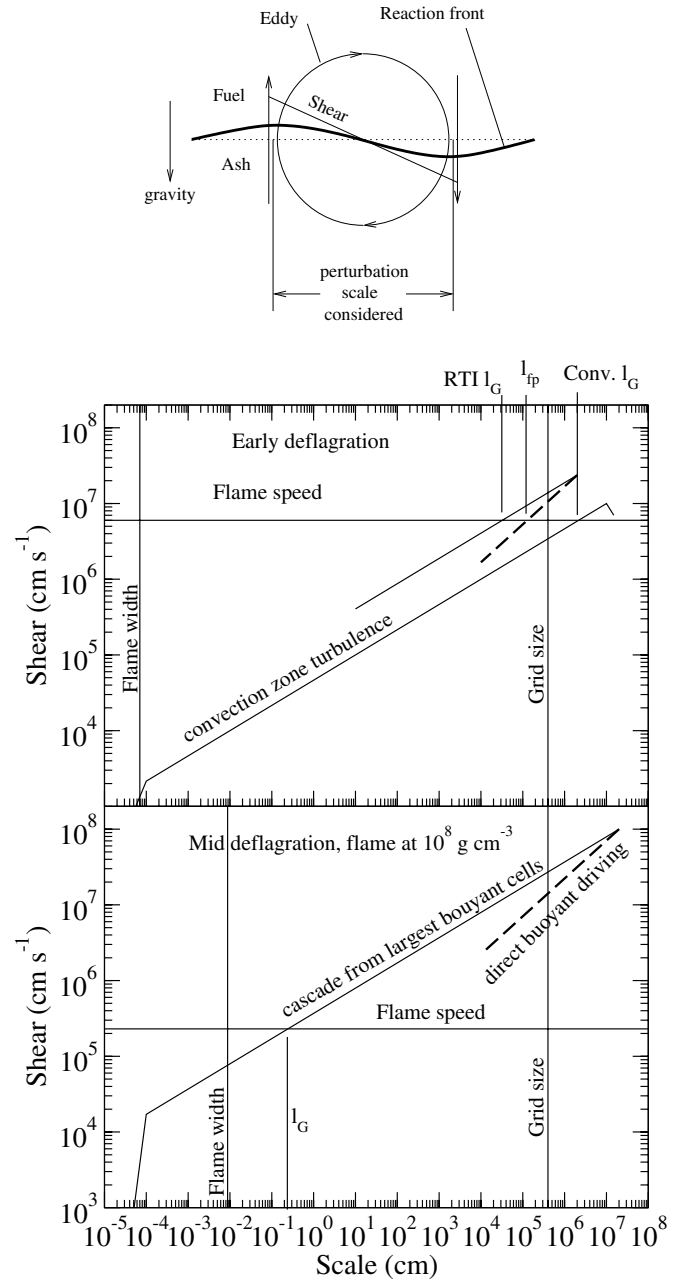


Figure 1. Top diagram: competing shearing contributions to wrinkling of flame front on some perturbation length scale. Bottom plots: shear strength from turbulence or buoyancy for perturbations to the flame surface on various scales two times during the deflagration, at early times (top) when $\rho \sim 2 \times 10^9 \text{ g cm}^{-3}$, and moderate times when $\rho \sim 10^8 \text{ g cm}^{-3}$. Solid lines indicate shear due to eddies in the turbulence cascade, while dashed lines indicate strength of buoyancy driving of moderate amplitude flame surface perturbations. Both of these vary with scale in the way shown. At early times two turbulence cascades are shown, the lower being the turbulence from the pre-deflagration convection zone, and the higher being due to the self-generated turbulence of the rising burned regions.

considered for arbitrary scale. An eddy in the fluid may wrinkle the flame by simply advecting adjacent parts of the front in opposite directions. Buoyancy will cause any perturbation of the type shown to grow in size due to the Rayleigh–Taylor instability (RTI). We wish to compare the strength of the shear given by each of these two processes with each other and with the flame propagation speed at a variety of scales and at different densities.

The flame is born in the core of the WD where $\rho \approx 2 \times 10^9 \text{ g cm}^{-3}$. At this high density, the flame is well-defined with a width $\delta_l \sim 10^{-4} \text{ cm}$. As the flame propagates into lower density material, the width increases and the flame become less well-defined, with disparity between the rate of C-fusion and the rate of other constituent reactions and the effect of turbulence becoming increasingly important (Timmes & Woosley 1992; Calder et al. 2007; Zingale & Dursi 2007; Aspden et al. 2008; Orvedahl et al. 2013). The flame width and speed at densities of $2 \times 10^9 \text{ g cm}^{-3}$ and 10^8 g cm^{-3} are shown by the left vertical line in the top and bottom plots respectively in Figure 1. The corresponding flame propagation speeds are shown by the horizontal lines in each.

The shearing characteristics of turbulence can be estimated from the approximate driving and the cascade. The convection zone is thought to be driven on scales $\sim 10^7 \text{ cm}$, or perhaps somewhat less, with rms speeds on that scale of order 10^7 cm s^{-1} (Woosley et al. 2009; Zingale et al. 2009). From this outer scale, the cascade will proceed toward smaller eddies, giving $v' \propto l^{1/3}$, the standard turbulence cascade, where v' can be used as a measure of the shear on a characteristic scale l .

The flame is subject to the effects of fluid instabilities and turbulence, both of which wrinkle the flame and thereby boost burning (Markstein et al. 1964). The subsonic burning front that begins near the center of a massive WD is subject to Kelvin–Helmholtz (KH), Landau–Darrieus, and RT instabilities (Khokhlov et al. 1997; Khokhlov 2000; Hillebrandt & Niemeyer 2000). The principal fluid instability influencing the flame is the RTI (Rayleigh 1882; Taylor 1950; Chandrasekhar 1981), occurring because the gradient of density across the flame is opposite the direction of acceleration of gravity. The evolution of the flame is also influenced by the KH shear instability (Helmholtz 1868a, 1868b; Thomson 1871) and the Landau–Darrieus instability (Darrieus 1938; Landau 1944; Pelcé 1988; Landau & Lifshitz 1987; Bychkov & Liberman 1995; Röpke et al. 2004) on scales similar to or smaller than those of the RTI.

The shear contribution to flame wrinkling due to RTI on some arbitrary scale l can be estimated by considering a perturbation like that shown in the top diagram in Figure 1. Ignoring curvature, the exponential growth rate of such a perturbation is $r = \sqrt{g_{\text{eff}}/l}$, where g_{eff} is the reduced gravity. For a modest perturbation, $\sim 0.1l$, like that shown in the figure, this can be converted to an effective shearing speed. $v' \sim lr = \sqrt{g_{\text{eff}}l}$. This allows a simple estimate of how the shearing (wrinkling) strength of the RTI depends on scale and allows an estimate to be made based on a typical plume size and gravity. This is shown by the thick dashed lines in Figure 1 for the early and middle deflagration epochs shown. In the early epochs, the plumes are expected to be only a few $\times 10^6 \text{ cm}$ across, while later they may reach sizes of several $\times 10^7 \text{ cm}$ or more as they rise into the outer parts of the WD, whose radius is about $2 \times 10^8 \text{ cm}$.

The RTI will also act as a driver of turbulence on all scales on which it is active. This turbulence will cascade to smaller scales via eddy break up. This buoyancy-generated turbulence is indicated in Figure 1 by the upper thin solid line in the upper plot and the single thin solid line in the lower plot. The shear due to the cascade from larger scales is generally stronger than the driving available from the RTI on that same scale. Note, however, that this is a steady-state view, and we are neglecting how the transient behavior through which this develops might behave.

Flame wrinkling is expected to cut off when $v' \lesssim s_l$, the laminar flame speed, as the flame propagation will smooth

out any induced wrinkles. For turbulence this is called the Gibson scale (Peters 1988, 2000; Niemeyer & Woosley 1997; Röpke et al. 2003; Aspden et al. 2008), the size of the smallest eddy, with a turnover velocity \gtrsim laminar flame speed. With a turbulence cascade that gives $v'(l) = V(l/L)^{1/3}$, this gives a Gibson scale of

$$l_G = L \left(\frac{s_l}{V} \right)^3, \quad (4)$$

where V is the velocity on some scale L , typically taken to be the driving scale, but can be taken as any scale in the inertial range of the turbulence. An analogous scale exists for the RTI, fire-polishing length

$$l_{\text{fp}} = 4\pi \frac{s_l^2}{g_{\text{eff}}}, \quad (5)$$

where g_{eff} is the effective gravitational acceleration (Timmes & Woosley 1992; Zingale et al. 2005b). The smallest scale of interest is the viscous dissipation scale, η_K , which in the case of the degenerate plasma of the WD is due to electron–ion collisions (Woosley et al. 2009), and is indicated by the downturn in the turbulence spectrum. This downturn is not included in the cascade from buoyancy at early times since the time-dependence of this development may be significant. The Gibson scale and the fire-polishing scale represent the smallest scale of wrinkling of the flame surface by turbulence and RTI respectively, since in all cases here they are larger than η_K .

As can be seen from Figure 1, the only time at which any of the Gibson scale, flame width, or fire polishing scales are resolved in a typical $\sim 4 \times 10^5 \text{ cm}$ resolution SN simulation is the Gibson scale for the flame subject to the pre-ignition convection field. As soon as any significant RTI takes place, both the Gibson scale and fire polishing scales are below the scale of the grid. The model presented here attempts to model the behavior of the flame between the resolved scale and the smallest wrinkling scale. It appears this inner scale will typically be the Gibson scale created by the cascade from the driving due to the largest buoyant cells. Eventually, in the late deflagration, as the flame width becomes even larger, this wrinkling scale will be smaller than the flame width, leading to strong distortion of the laminar flame structure and possibly a deflagration to detonation transition.

In all conditions the main driving of the turbulence being modeled, pre-existing convection, RTI, and large KH scales related to the RTI plumes, are on scales far enough above the grid scale that the cascade should be able to be characterized on resolved scales well enough to infer the subgrid structure of the cascade. One possible exception is KH effects which may also drive turbulence from smaller scales more similar to the flame surface scale, which is unresolved. The TFI models discussed here are intended to model the extension of turbulence to subgrid scales. Thus as long as the driving scales are sufficiently larger than the grid scales for the turbulence cascade to be properly measured, changes in the driving scale should be accounted for.

2.4. Flame Models

It is convenient to introduce two immediate abstractions that are closely related to the flame modeling techniques that will be discussed shortly. One is to define some form of reaction progress variable. We will use ϕ , which varies, for example, from 0 to 1 from the fuel to the ash. The flame is then defined by a field ϕ at every point in space. This definition abstracts

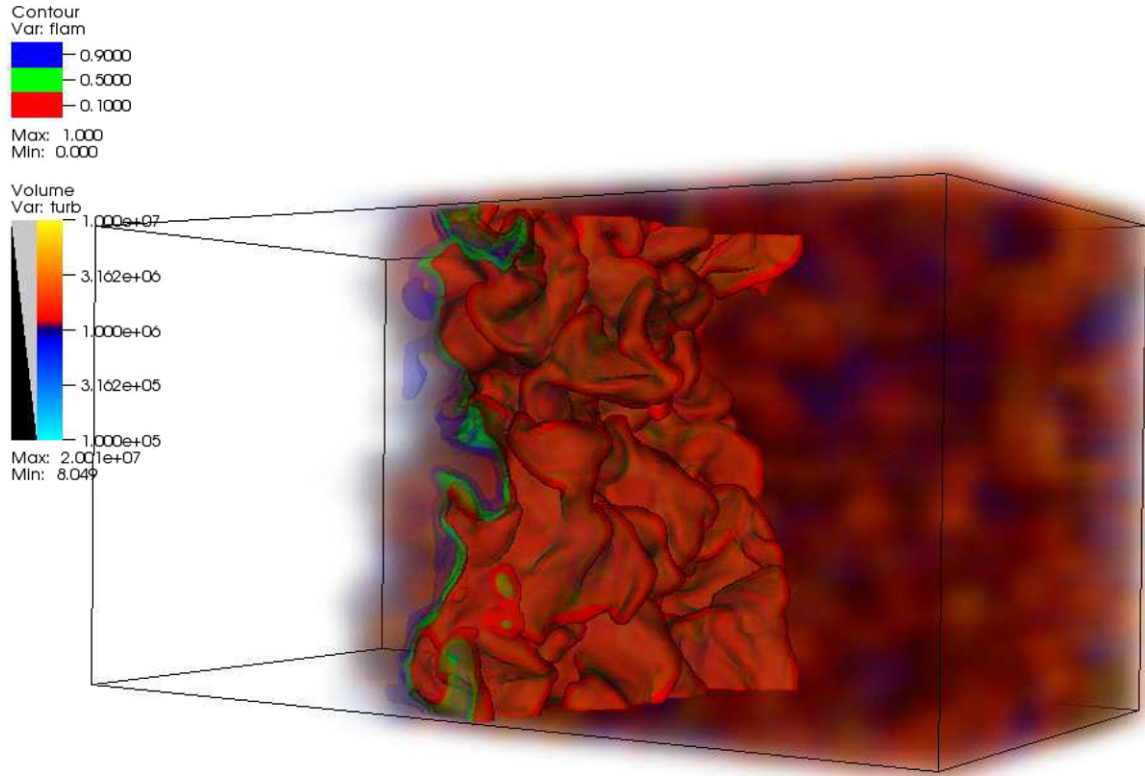


Figure 2. Iso-surface of the reaction progress variable at $\phi = \{0.1, 0.5, 0.9\}$ (red, green, and blue, respectively) for a reaction-diffusion model flame. The volume rendering indicates the turbulent strength with stronger turbulence in orange and weaker in blue. An initially laminar flame propagating at 10 km s^{-1} interacts with decaying turbulence with an initial rms velocity of 100 km s^{-1} . The channel width is 15 km .

(A color version of this figure is available in the online journal.)

away much of the detail of the flame structure, including the distinction between its thermal and compositional structure, though ϕ can be taken to represent some aspect of one of these two. A second layer of abstraction can be introduced (conceptually or explicitly) by representing the flame as an isosurface, say $\phi = 1/2$. The (thick-)surface-like region can be highly wrinkled by fluid advection, as shown in Figure 2 which shows a model flame (a reaction-diffusion front) propagating in a turbulent fluid. The isosurfaces show regions near the “forward edge” of the flame ($\phi = 0.1$) and the “back edge” ($\phi = 0.9$), and demonstrate that the reaction region as a whole is fairly well characterized by a slightly thickened wrinkled surface. What is meant by the thickness of the region and its detailed structure is not universal, and will depend on what features are being modeled versus being simulated directly. Several examples will be given below.

The turbulence in SNe Ia and its relation to and interaction with the flame provides several challenges. First, the Reynolds number (Re) characteristic of combustion in a degenerate WD is practically infinite ($\sim 10^{14}$), which implies that $\ell_t \gg \eta_k$, where ℓ_t is the integral scale of the turbulent cascade and η_k is the dissipation scale due to electron-ion collisions (Woosley et al. 2009). In fact, even for the weak turbulence present when the flame ignites ($v'_i \sim s_l$, where v'_i is the rms velocity fluctuation on the integral scale and s_l is the speed of the flame in laminar flow), η_k is typically smaller than the laminar flame width, $\eta_k < \delta_l$. This characteristic presents an important distinction from laboratory flames, where, for weak turbulence $\eta_k > \delta_l$. Thus while in laboratory flames under weak turbulence, there simply are no eddies active on scales similar to or smaller than

the flame thickness. In astrophysical flames, however, there are always slight perturbations to the reaction zone from eddies on these scales.

In addition, the timescale for the explosion is $\sim 1 \text{ s}$, while the timescale for turbulence at the integral scale at ignition is comparable at $\sim 2\text{--}20 \text{ s}$ (Zingale et al. 2009). The timescale for turbulence is expected to speed up quickly as driving from the RT KH fluid instabilities result from burning cold, dense fuel to hot, light ash in the deep gravitational well of the degenerate WD. All the while, the star is expanding due to the release of nuclear binding energy, increasing the mean velocity of the fluid elements, which serves to dampen the turbulent velocity fluctuations in relative terms. All of these competing processes on the fluid flow occur on similar timescales, which should not allow one to assume equilibrium turbulence. However, due to the necessity to treat unresolved structure in fluid flow and the lack of availability of an appropriate model, turbulence is almost always assumed to be in equilibrium on subgrid scales. This assumption allows for analytic expressions for the time-averaged behavior of the unresolved turbulence as a function of resolved, larger-scale turbulent fluctuations. Despite the need for a non-equilibrium, non-Kolmogorov model for unresolved turbulence, development efforts are still in their infancy, at least in the context of SNe Ia.

For SN Ia simulations, we are primarily concerned with the effect the turbulence has on flame propagation. The modeled flame should respond appropriately to the unresolved modeled turbulence, in addition to the explicit fluid flow (resolved turbulence) in the simulation. Due to their close relationship in implementation, in a general context the term “TFI model”

will include both a model of turbulence and its interaction with the flame, because both must be specified. However, for this work we will mostly make a distinction between the turbulence model and the TFI, and use the latter term for the portion of the model that directly addresses effects on the flame.

While the RT and KH instabilities play an important role in generating flame surface in SNe Ia, the inclusion of their combined effects into a self-consistent model for under-resolved turbulent combustion is a difficult problem (Khokhlov 1995; Schmidt et al. 2006b; D. M. Townsley et al. 2008, private communication) that we will not address in this work. This choice is partly due to the desire to assume homogeneous, isotropic turbulence, which is well described by Kolmogorov turbulence theory (Kolmogorov 1941, 1991), and provides a starting point for treating TFI. The inclusion of either the RT or KH instabilities breaks the assumption of isotropy, and greatly increases the complexity of the theoretical model; however, these inclusions may not be necessary provided the simulation is sufficiently well-resolved (Zingale et al. 2005a; Ciaraldi-Schoolmann et al. 2009).

2.5. Types of Flame Models

A variety of applicable approaches have been used to model flames (Driscoll 2008; Poinot & Veynante 2005), which we will not attempt to review here in detail. Instead we focus the discussion toward the differences between artificially thickened flames and flame front tracking methods, because this difference is important for our adaptation of the work in CVDP and CMV to astrophysical flames. Artificially thickened flames model the combustion with similarity to the physical processes, with “simple chemistry” using an Arrhenius law, and thermal and chemical diffusion. However, the reaction rate and molecular and thermal diffusivities are increased by a thickening factor, such that the real flame structure is resolved on the computational domain but the propagation speed is unchanged (O’Rourke & Bracco 1979). On the other hand, flame front tracking methods (used in astrophysics) such as the G -equation (Schmidt et al. 2006a) and advection-reaction-diffusion (ARD or ADR) equation (Khokhlov 1995), do not attempt to reproduce physical features of the flame structure.

The thickened flame approach has the advantage of incorporating various phenomena naturally, such as effects due to flame curvature and stretch, by using the Arrhenius law. This is due to the fact that the basic physical flame structure is retained, including the pre-heat zone and the reaction zone. This structure is especially important for astrophysical flames in which the Lewis number (Le) is nearly infinite, i.e., thermal diffusion dominates over species diffusion. For large Le , the local propagation speed depends strongly on curvature, due to the focusing or de-focusing of heat by thermal conduction. This approach works well when the thickening factor is not too large, such that not much flame structure can hide on unresolved scales; however, for large thickening factors, it is not obvious that the thickened flame structure represents the average behavior of the flame on unresolved scales, particularly when turbulence is moderately strong. The model flame in this case will be strained and stretched by the turbulence at the scale of the computational domain, and the resulting nonlinear burning rate is likely to be much larger than that expected from the physical flame.

A thickened flame approach would have disadvantages for the SN Ia full-star explosion simulations. For our simulations of SNe Ia, the laminar flame width is under-resolved by a factor ranging 10^6 – 10^{10} . In this case, we do not expect the model flame

structure to behave the same way as the physical flame on these scales. Curvature effects that should not be important for weak turbulence will be unduly promoted into severe effects by the artificial thickening of the flame. In addition, a single thickening factor would not be appropriate for the entire range of physical conditions treated during the explosion. The range of physical flame widths varies by many orders of magnitude (Chamulak et al. 2007; Timmes & Woosley 1992). For small thickening factors, it is advantageous to have some of the physical features of flames, such as curvature effects, directly simulated. For large thickening factors these effects are more appropriately moved into the model for the flame dynamics where they can be controlled and introduced when they are physically relevant.

In order to avoid undesirable issues with a thickened flame, it is useful to substitute a relatively artificial structure for the reaction front; preferably one that does not respond strongly to strain and stretch. This is necessarily a coarse structure, since it must be resolved in the simulation. We use an ADR equation to define a propagating reaction front that represents the flame front, with the reaction and diffusion terms determined dynamically to provide a desired front-propagation speed and interface width (see Khokhlov 1995; Vladimirova et al. 2006; Townsley et al. 2007, 2009). Rather than having a peaked energy-generation rate in the reaction zone as with the Arrhenius law, the energy generated from combustion is smoothly distributed over the interface. This approach has the advantage of having been demonstrated to produce an acoustically quiet flame front (Townsley et al. 2007). Additionally, the propagation is effectively due to species diffusion rather than thermal diffusion; however, it is important to note that the ADR scheme is not intended to represent physical flame structure. Another alternative, based on methods widely applied in the combustion literature and applications is that of the G -equation (Reinecke et al. 1999; Röpke et al. 2003, also called “level-set”), in which the interface surface between fuel and ash is reconstructed explicitly on the grid and then propagated using the advection of an appropriately defined scalar field. This case has the advantage of being effectively as thin as possible, presenting a challenge of what to do at the interface (Röpke et al. 2003), but still is limited to representing a coarse surface structure. For the level-set approach as implemented by Reinecke et al. (1999), the artificial front is known to produce spurious velocity oscillations due to the approximations adopted in the “passive” implementation defined in that work and used in astrophysical simulations.

In any case, a model is required to inform the artificial reaction front how fast to propagate given local conditions such as the local thermodynamic quantities, composition, and turbulent intensity. Each approach has its own advantages and disadvantages as summarized above. We choose to employ the ADR scheme to both minimize numerical noise and minimize curvature and strain effects compared to a thickened flame. Utilizing an acoustically quiet model flame is important in the context of TFI models to minimize the possibility of providing feedback into the turbulence measure. While such feedback effects may be possible, they should be well-controlled and described in the TFI model.

2.6. TFI Models Used for SNe Ia

In this work we describe a method to enhance the laminar front propagation speed of our model flame. This method is composed of two parts: measuring the SGS turbulent intensity (Section 4) and estimating the turbulent flame speed from the turbulent intensity (Section 5). We utilize an instantaneous, local

measure of the SGS turbulent intensity from the resolved fluid flow and a TFI model that accounts for inefficient wrinkling of the flame which will occur at low densities. As a prelude, this section provides some context of how our choices relate to and are motivated by previous work on TFI for SNe Ia.

Treatment of flames in multidimensional simulations of SNe Ia have followed basically two lines of development, beginning generally from work of Niemeyer & Hillebrandt (1995) on one hand and Khokhlov (1995) on the other. From the standpoint of TFI, these can be grossly characterized as explicit and implicit respectively, though the latter does have an explicit model for RT effects. Our use of “implicit” is in the sense of implicit large eddy simulation of fluids, in which viscous dissipation is left to numerical effects (finite resolution) without inserting an explicit numerical viscosity from a defined model of SGS turbulence (see, e.g., Aspden et al. 2011). In this way “implicit” means that salient features are assumed, for at least some portions of parameter space, to transfer to the grid scale in a way which does not change the gross simulation outcome. We will not discuss implicit methods in any more detail here, as this work is concerned with the development and exploration of explicit TFI, for which we have specific concerns, outlined below, in relation to previous work on that topic.

Continuing work outlined by Niemeyer & Hillebrandt (1995), Schmidt et al. (2006a, hereafter SNH) recently developed an SGS model to account for under-resolved TFI and applied it to SNe Ia with the inclusion of under-resolved RT modes in Schmidt et al. (2006b, hereafter SNHR). Part of the motivation for the present study is out of interest in understanding the impact of some of the modeling choices made in SNH on the results presented in SNHR and subsequent work (e.g., Seitzzahl et al. 2011). SNH developed a detailed model of SGS turbulence, which separately treats the creation, transport and dissipation of SGS turbulent energy. While this model is a major advancement in the treatment of TFI as it allows for the quantification of SGS turbulence, several features of the model are concerning in the context of SNe Ia that must be discussed.

First, we outline our concern with the posited diffusive term in the SNH SGS turbulence model. In the process of calibrating their closure relations, SNH demonstrated that computing the diffusion of SGS turbulent energy via gradient-diffusion yields an incorrect estimate of the direction of diffusive flux. When directionality is considered using a dot product between the gradient direction and the computed flux of SGS turbulent energy, as in SNH, Equation (77), the resulting calibrated closure parameter underestimates the magnitude of diffusive flux by an order of magnitude. On the other hand, when directionality is ignored, as in SNH, Equation (78), the resulting calibration demonstrates that the magnitude of the gradient in SGS turbulent energy is an excellent predictor of the magnitude of the actual flux. Together these imply that, on average, only $\sim 10\%$ of the flux of SGS turbulent energy is directed in the gradient direction. There is no clear way to go about finding the direction of the diffusive flux from coarse quantities (but see SNH for references to some work in this direction.) Thus, in order to use the gradient-diffusion method, SNH must choose how much flux to send in the gradient direction. They choose to set the closure parameter—the coefficient of the diffusive flux term—to the value which gives the correct magnitude of the SGS turbulent energy flux, resulting in a turbulent kinetic Prandtl number of order 10 (extremely diffusive). However, inverting the implications discussed above, this overestimates the flux in the gradient direction by an order of magnitude.

Our concern for transport of SGS turbulent energy in the gradient direction is of particular interest for the SN Ia problem. From SNHR, Figures 4–6, the magnitude of SGS turbulent energy moved by diffusion is comparable to production, and production occurs mostly in the ash behind the flame. Our concern is that the direction of gradient-diffusion is computed to generally align with the direction of flame propagation (since turbulence is generated behind the flame front), and the spread of the flame may be dominated by turbulence diffusing from behind the flame to the flame front. This is quite likely to be the proper physics, at least in certain portions of the flame. However, according to the tests of gradient-diffusion presented in SNH, the magnitude of this effect may be over predicted by a factor of 10 in their SGS model.

Finally, we must point out that SNHR utilize an implementation of the level-set method to describe their model flame, which is known to produce oscillations in the velocity field near the flame front (Reinecke et al. 1999), and was demonstrated to have poor stability of the flame surface (Röpke et al. 2003). It is not known whether the turbulence generated by this noise is captured by their SGS turbulence model or how significant the effect might be.

It is not established that such a detailed model of SGS turbulence is necessary for treatment of TFI in the SN Ia. The spread of resolved turbulence across the grid might be a sufficient quantification of this effect, without requiring the invocation of a model. As discussed in CVDP, on which our measurement of unresolved turbulence presented in Section 4 is based, it is not obvious how to translate quantities in an SGS turbulence model into an appropriate “measure” of turbulence that will interact with the flame. In particular, any determination of turbulence must evaluate to zero in the limit of a perfectly laminar flame. As a result, even for simulations which include an SGS turbulence model, CVDP prefer a separate operator for TFI specifically constructed to filter out effects due to thermal expansion of the reacted products. (See Section 4 for continued discussion.)

The second way in which we attempt to improve treatment of TFI for SNe Ia is to improve the way in which high turbulence intensities—or equivalently low laminar flame speeds—are handled. SNHR assume the interaction between the flame front and turbulence is scale invariant (Pocheau 1994), so that the flame can wrinkle arbitrarily finely in response to turbulence. However, for high-intensity turbulent combustion, the turbulent flame speed has not been observed to scale with the turbulent intensity (Abdel-Gayed & Bradley 1981). The approximation of scale invariance for TFI in degenerate WDs seems to be appropriate near the core where the density is high and the ratio of turbulent intensity to the laminar flame speed is relatively low; however, as the flame propagates to lower densities and approaches conditions predicted for DDT, this approximation is no longer valid. This effect has been handled in previous simulations in an approximate way by inserting a density cutoff in the flame propagation. The TFI models we are adapting, CVDP and CMV, are constructed to allow for inefficient wrinkling, and evaluate this effect based on flame–vortex interaction efficiencies evaluated with DNS of unity-Le flames. This improvement is less likely to have a direct effect on explosion outcomes, only becoming important at late times near the DDT, but may be important for properly localizing the DDT site. It will also be important in future work to incorporate results from DNS studies of flame-turbulence interactions that are specific to the flame in SNe Ia (Aspden

et al. 2008, 2010, 2011) as an improvement over the more general vortex–flame interactions for simple reactions studied by CVDP. Improved modeling of flame–vortex interaction in the later stages of the deflagration may be particularly relevant to understanding situations in which the DDT might fail (Jordan et al. 2012b; Kromer et al. 2013).

3. OVERVIEW OF FLASH

This manuscript concerns the implementation of a TFI model to describe SGS processes unresolvable in full-star, 3D simulations of SNe Ia using the FLASH code, version 3. In order to properly implement the model, FLASH is also used to generate turbulence fields and propagate test flames in simplified geometries. Full details of the numerical code can most recently be found in Townsley et al. (2009) and work referenced therein, but an overview is provided here for completeness. FLASH is a Eulerian compressible adaptive-mesh hydrodynamics code (Fryxell et al. 2000; Calder et al. 2002). FLASH uses a high-order shock-capturing compressible hydrodynamics method, the piecewise parabolic method (PPM, Colella & Woodward 1984), adapted to treat a general equation of state (EOS, Colella & Glaz 1985). We use a tabulated fully-ionized electron–ion plasma EOS (Timmes & Swesty 2000; Fryxell et al. 2000) appropriate for conditions in the degenerate core of a massive WD. FLASH supports using this hydrodynamics method on an adaptively refined, tree-structured, non-moving Eulerian grid. Several modifications have been incorporated to perform simulations of SNe Ia including a nuclear burning model, updated flame model with composition-dependent input laminar flame speeds, and specific mesh refinement criteria (for details, see Calder et al. 2007; Townsley et al. 2007, 2009; Jackson et al. 2010). While the utilization of adaptive mesh refinement is critical for simulations of SNe Ia, FLASH also supports a uniform grid, which we use for generating turbulence and propagating flames in test channels.

As motivated above, the unresolved flame is modeled by a resolved reaction-diffusion front in which a progress variable, ϕ , varies from 0 to 1 as burning proceeds. Reaction and diffusion act on the same variable, so that the dynamics are given by

$$\frac{\partial \phi}{\partial t} + \mathbf{v} \cdot \nabla \phi = \kappa \nabla^2 \phi + \frac{1}{\tau} R(\phi), \quad (6)$$

where $R(\phi)$ is a reaction function, \mathbf{v} is the fluid velocity and the coefficients κ and τ are chosen along with R to maintain a resolved reaction front width and the desired spatial propagation speed. Energy is released linearly with ϕ in our test simulations and as described in Townsley et al. (2007) in SN simulations. How the speed should be chosen is addressed in this work as discussed below. All components implementing reaction-diffusion and turbulence measurement used in this work, including test simulations presented in Section 6.3, will be available in the 4.2 release of the FLASH Code.

4. MEASURING UNRESOLVED TURBULENCE

In this section we outline and calibrate a local differential operator that will quantify the strength of turbulence at any given region on the grid. This will form an input to the TFI model described in Section 5. Our “model” of SGS turbulence, such as it is, is simply a Kolmogorov cascade whose local strength at a scale Δ just above the grid scale Δ_x , is based on the operator outlined here. Thus, we implicitly assume that the SGS turbulent velocity field is homogeneous and isotropic on scales

smaller than approximately Δ and does not vary significantly in strength on timescales shorter than the eddy turnover time at the grid scale. This model, though simple, will be used explicitly in evaluating how the TFI wrinkles the flame. As discussed in detail in Section 2 our model of turbulence is chosen to complement other approaches such as that of SNHR, which instead have a detailed *dynamical* model for SGS turbulence creation, transport and dissipation.

We want to measure resolved turbulent motions that are not caused by the expansion of material as it is burned. This component of turbulence can be argued to exist ahead of a propagating burning front such that it wrinkles the front and influences the local burning rate. CVDP describe a finite-difference operator “ OP_2 ” to measure resolved turbulence with the irrotational velocity component filtered out

$$OP_2(\mathbf{u}) = (h\Delta_x)^3 |\nabla \times (\nabla^2 \mathbf{u})|, \quad (7)$$

$$u'_\Delta = c_2^h OP_2(\mathbf{u}), \quad (8)$$

where u is the velocity vector field, c_2^h is a constant, calibrated below, such that u'_Δ represents the turbulence on unresolved scales ($< \Delta$), and h is the index of the stride in the finite difference scheme (an integer, typically 1 or 2). The irrotational component is filtered out in order to prevent the expansion inherent in the flame from contributing to the measurement. The constant c_2^h is determined by requiring that the kinetic energy of the turbulent velocity measured be equal to the kinetic energy contained in the turbulent cascade between Δ and the physical dissipation scale (η_k). The length scale Δ is a characteristic of the operator, and therefore depends on h and Δ_x . Because the dissipation range of resolved turbulent flows begins well above the grid scale, the length scale Δ associated with the turbulence operator typically lies within the dissipation range. Therefore, c_2^h serves partially to correct for the effects of numerical dissipation. This formulation allows some flexibility in Δ by choosing different values for the integer stride h . In general, c_2^h will depend on the choice of h and the numerical method used to evaluate Equation (7) and the particular form the numerical dissipation takes (see Sytine et al. 2000 for more details about numerical dissipation with PPM). We use a fourth-order finite central difference with

$$\frac{\partial f}{\partial x} = \frac{f_{i-2h} - 8f_{i-h} + 8f_{i+h} - f_{i+2h}}{12h\Delta_x} \quad (9)$$

$$\frac{\partial^2 f}{\partial x^2} = \frac{-f_{i-2h} + 16f_{i-h} - 30f_i + 16f_{i+h} - f_{i+2h}}{12h^2\Delta_x^2}. \quad (10)$$

For this particular implementation, the length scale associated with the turbulence operator is approximated by $\Delta = 4h\Delta_x$, because the turbulence measured in a particular cell uses velocity information from cells up to $4h$ cells away. Other definitions of Δ could be adopted which would affect the calibration of c_2^h essentially rescaling the distribution of OP_2 to agree with the expected value at scale Δ .

For FLASH, we calibrate c_2^h using a Kolmogorov turbulence cascade generated by driving fluid motions on large scales. We drive turbulence in a triply-periodic Cartesian box with varying resolutions for 1.5 eddy-turnover times (τ_e), where $\tau_e = L/v_{\text{rms}}$, $L = 1.5 \times 10^6$ cm is the size of the box, and v_{rms} is the root-mean-squared velocity of the resolved flow. We follow the simulation setup `StirTurb` distributed with FLASH (Fisher et al. 2008), except that we use a degenerate equation

Table 1
Measured Values for c_2^h for Various Resolutions N with v_{rms}

N	128	256	512	1024	c_2^h
$c_2(h=1)$	0.69	0.79	0.92	0.97	0.9
$c_2(h=2)$	0.24	0.27	0.30	0.31	0.3
v_{rms} (km s $^{-1}$)	685	680	685	687	

of state, the same as that used for our simulations of SNe Ia, with $\rho = 7.3 \times 10^7$ g cm $^{-3}$ and $T = 4.3 \times 10^9$ K. We drive the turbulence at a scale $L/3$ with an energy to achieve $v_{\text{rms}} \approx 0.1c_s$, where $c_s \approx 6 \times 10^8$ cm s $^{-1}$ is the sound speed. The turbulence cascade for all simulations converge to a single steady-state profile in phase space by $t = 1.5\tau_e$.

We want to correct for numerical dissipation, so we construct an idealized specific kinetic energy cascade that follows the well-known $-5/3$ power law for steady-state, homogeneous and isotropic turbulence, i.e., $E(k) = Ak^{-5/3}$ erg cm g $^{-1}$, where k is the norm of the vector wavenumber and A is a proportionality constant. This energy function represents the turbulence we would expect if we had infinite resolution (and no numerical dissipation). Intermittency is also being ignored and corrections should be minor. By definition, integrating the energy function over all wavenumbers yields the total kinetic energy per unit mass. Because our idealized energy function is only valid between the integral scale (ℓ_t) and η_k and most of the energy is contained at the integral scale, we choose to solve for A by approximating the integral over all wavenumbers to those between $2\pi/\ell_t$ and $2\pi/\eta_k$

$$\int_{2\pi/\ell_t}^{2\pi/\eta_k} E(k) dk = \frac{1}{2} v_{\text{rms}}^2, \quad (11)$$

where $\ell_t = L/3$, the scale at which turbulence is driven. For the astrophysical flows of interest, $\text{Re} \sim 10^{14}$ such that $\eta_k \ll \ell_t$, and therefore, we take the upper bound of the integral to infinity. Then, defining $k_{\text{drive}} = 2\pi/\ell_t$, A becomes

$$A = \frac{1}{3} v_{\text{rms}}^2 k_{\text{drive}}^{2/3}, \quad (12)$$

where v_{rms} is given in Table 1 for all simulations. One could also choose to solve for A by choosing an ‘‘anchor’’ value within the inertial range of the cascade, but because an inertial range is present only for the higher 512 and 1024 cell simulations, this method may not be consistent for all cases.

By analogy with v_{rms} , we want u'_Δ to represent the turbulent energy on unresolved scales, $E_{\text{SGS}}(u'_\Delta) = u'^2_\Delta/2$. So instead of integrating from the driving scale, we integrate from the wavenumber corresponding to the length scale associated with the turbulence operator, $k_\Delta = 2\pi/\Delta$

$$E_{\text{SGS}}(v_{\text{rms}}, \Delta) = \int_{k_\Delta}^{\infty} E(k) dk = \frac{1}{2} v_{\text{rms}}^2 \left(\frac{k_{\text{drive}}}{k_\Delta} \right)^{2/3} \quad (13)$$

The calibration constant is then derived from the desire for $\langle E_{\text{SGS}}(u'_\Delta) \rangle = E_{\text{SGS}}(v_{\text{rms}}, \Delta)$,

$$(c_2)^2 = \frac{2E_{\text{SGS}}}{\langle OP_2(\mathbf{u}')^2 \rangle} = \frac{v_{\text{rms}}^2}{\langle OP_2(\mathbf{u}')^2 \rangle} \left(\frac{k_{\text{drive}}}{k_\Delta} \right)^{2/3}. \quad (14)$$

While $\langle \dots \rangle$ is most appropriately an ensemble average (Davidson 2004), in the analysis below we use spatial averages over all

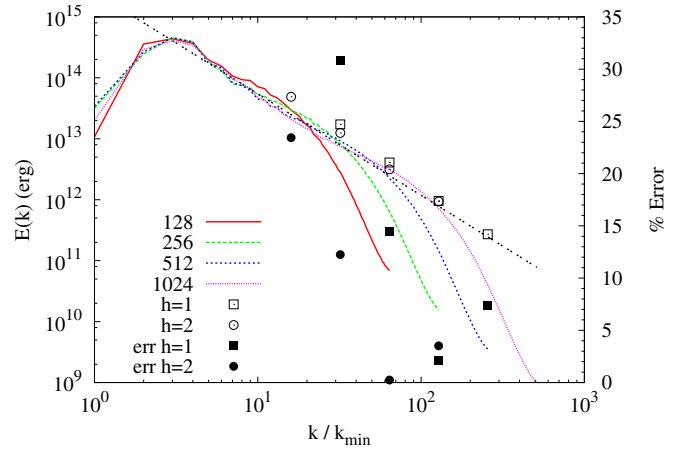


Figure 3. Spectral energy content of stirred turbulence in a cubic periodic box of size L for four different resolutions that range 128–1024 computational cells along each dimension as a function of wavenumber in units of $k_{\text{min}} = 2\pi/L$. The open points show $E(k = k_\Delta)$, the energy contained in the length scale Δ (for different integer strides h), as inferred from the turbulence measurement operator (see text for details). The dashed line is computed from v_{rms} with $E(k) = Ak^{-5/3}$ and Equation (12) showing the expected $-5/3$ power-law. Because each resolution results in a slightly different calibration for c_2^h , we choose one representative value (provided in Table 1) and show the error in the turbulent intensity with filled points associated with the right y-axis using Equation (15).

(A color version of this figure is available in the online journal.)

points in an assumed homogeneous box. Here, OP_2 is log-normally distributed, as expected, with the standard deviation being $\approx 5\%$ of the mean in log-space.

Figure 3 shows the spectral energy content for four different resolutions, $N = 128, 256, 512,$ and 1024 cells along each direction. The energy spectra, $E(k)$, are computed by taking the Fourier transform of the velocity field and binning energy in spherical shells of wavenumber $k = \sqrt{k_x^2 + k_y^2 + k_z^2}$. The Fourier transforms are computed using the publicly available FFTW routines, with an additional multiplicative normalization factor of $1/N^3$. From the energy spectrum, the driving scale can be discerned as $k_{\text{drive}} = 3k_{\text{min}}$, as specified from $E(k) = Ak^{-5/3}$ and Equation (12) with v_{rms} from the 1024-resolution simulation given in Table 1. The large dissipation range can be observed, with a well-defined inertial range only evident at $N = 512$ and 1024 . These also display the expected ‘‘bump’’ in the power spectrum between the inertial and dissipation ranges (Sytine et al. 2000).

Each resolution results in a slightly different value for c_2^h , and these are presented in Table 1. This is expected because the nature of the dissipation range is known to depend on the overall resolution (Fisher et al. 2008; Aspden et al. 2011). We choose a representative value for each h , given in the last column of Table 1, and use this as our calibrated c_2^h . Using this calibrated constant, the open points in Figure 3 show what the turbulent operator infers the energy to be at k_Δ , where $E(k_\Delta) = 2E_{\text{SGS}}(u'_\Delta)/3k_\Delta$. We show the error in the inferred turbulent intensity, incurred by using a single, resolution-independent value for c_2^h , with filled points associated with the right y-axis, where the error is given by

$$\% \text{ err}(u'_\Delta) = \frac{\text{abs}(u'_\Delta - \sqrt{2E_{\text{SGS}}(v_{\text{rms}}, \Delta)})}{\sqrt{2E_{\text{SGS}}(v_{\text{rms}}, \Delta)}} \times 100, \quad (15)$$

which reduces to

$$\% \text{ err}(u'_\Delta) = \text{abs} \left(\frac{c_2^h}{c_2^h(N)} - 1 \right) \times 100. \quad (16)$$

The error is found to be modest (less than 15%) for a cascade that is moderately well-captured on the grid, i.e., for resolutions of 256 and above. Even at lower resolutions, errors of 30% are likely to be fairly benign assuming that an important portion of the TFI is contained in the resolved scales. Uncertainties of similar magnitude exist in the calibration method itself. By choosing to “anchor” A with an energy value within the inertial range, c_2^h for all cases drops by ≈ 0.1 , resulting in a $\sim 10\%$ decrease for $h = 1$ and $\sim 40\%$ decrease for $h = 2$.

The calibration of c_2^h presented in this work is different from CVDP for a couple of reasons. First, CVDP absorb the h factor into c_2^h whereas we include it explicitly in OP_2 in order to recover the appropriate scaling with length Δ . Additionally, CVDP use $h = 2$ for a second-order finite central difference approximation to the Laplacian, while using $h = 1$ for the curl.

With the operator presented and calibrated here, we can form an instantaneous model for the turbulence on unresolved scales. This model consists of a Kolmogorov cascade in which the overall magnitude of flow velocities as a function of scale provides a smooth continuation of the cascade from the resolved inertial range. Though the velocity structure is measured in the dissipation range, this has been compensated for in order to provide a continuation of the inertial range. With an additional model for how a flame wrinkles in the presence of a Kolmogorov-like velocity spectrum, we will be able to derive the behavior of the flame on subgrid scales. This topic is pursued in the following sections.

5. TURBULENCE–FLAME INTERACTION MODEL

A TFI model estimates the turbulent flame speed from the characteristics of the turbulent cascade and the laminar flame. For the TFI models discussed in this work, we limit our analysis to combustion regimes in which the flame is a well-defined concept. Generally for application to LES, TFI is concerned with accounting for subgrid flame structure that enhances flame propagation above what the resolved, and therefore necessarily smooth, reaction front achieves. Models therefore predict the front propagation speed of the reaction front resolved on scale Δ , or the effective turbulent flame speed of the coarsened reaction front, $s_{t\Delta}$.

5.1. Expectations and Model Construction

We implemented a few models based on CVDP and CMV, finally deciding that CMV is most complete and appropriate, out of those considered here, for simulations of SNe Ia with FLASH. After some preliminary studies concerning how the models are constructed, our adaptation of the power-law flame wrinkling model of CMV is given in Section 5.2. After this, as a supplement, we briefly discuss our attempts to directly adapt CVDP which result in unsatisfactory models. While we summarize the approaches here, see CVDP and especially CMV for a full description.

It is first useful to outline some expectations for our model from general principles and known scaling laws. Turbulent flames are often characterized by a wrinkling factor Ξ , often defined as $\Xi \equiv A_t/A_l$, such that $s_t = \Xi s_l^0$, where s_t is the turbulent flame speed, A_t is the surface area of the turbulent

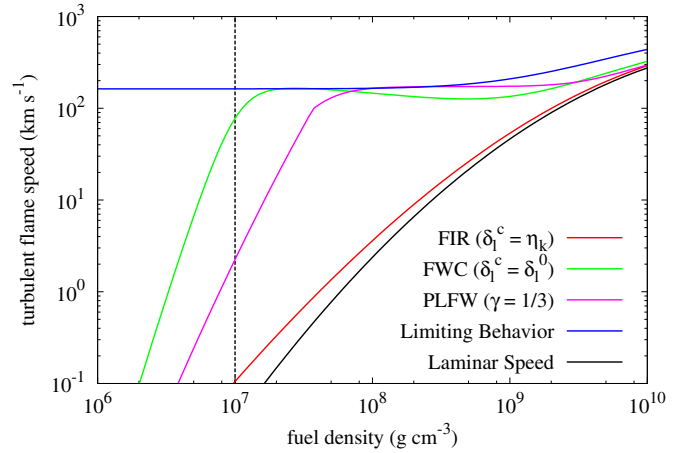


Figure 4. Turbulent flame speed is estimated using a simple Kolmogorov cascade constructed with $u' = 300 \text{ km s}^{-1}$ and $\ell_t = 100 \text{ km}$, where both the laminar flame speeds and widths are log–log fits as functions of density for a 50/50 C–O fuel mixture from Chamulak et al. (2007) with $\text{Pr} = 10^{-5}$. The red and green lines are constructed using the Full Inertial Range (FIR) and GS models with Equations (28) and (29). The blue line shows the limiting behavior with $\Xi_\Delta = 1 + u'_\Delta/s_l^0$, while the black line is the fitted laminar flame speed as a function of fuel density. For comparison, results from the power-law flame wrinkling model using a $\gamma = 1/3$ power-law are shown in magenta. In all cases, $\Delta = 16 \text{ km}$. The cut-off to $s_{t\Delta}$ that has typically been used in previous models occurs at the suspected transition away from the flamelet regime (vertical dashed line) (Schmidt et al. 2006b; Townsley et al. 2007).

(A color version of this figure is available in the online journal.)

flame, and A_l is the surface area of the laminar flame. For clarity, we are following the convention in CVDP and using s_l^0 for the laminar flame speed of the physical flame, for which we have simply used s_l in previous sections. This is intended to contrast with s_l^1 , which would be the speed of the thickened or artificial flame, which is our ADR front. The wrinkling factor describes the increase in flame surface area due to turbulence. We leave the length scale on which this might apply slightly abstract for the moment. One well-known scaling law is Damköhler scaling, in which, for moderately strong turbulence, the average flame speed $s_t \approx u'$, where u' is the characteristic turbulence intensity. One way to parameterize this scaling is to suggest a wrinkling factor of the form

$$\Xi = 1 + \beta \frac{u'}{s_l^0} \quad (17)$$

where β is a constant of order 1. For the SN Ia, the physical laminar flame speed, s_l^0 is strongly dependent upon fuel density. It is therefore convenient to consider the dependence shown in Figure 4, where s_t is plotted against density for a given turbulence field. In keeping with the rest of the discussion, we emphasize $s_{t\Delta}$, the enhancement to subgrid propagation. A simple Kolmogorov cascade is assumed with $u' = 300 \text{ km s}^{-1}$ and $\ell_t = 100 \text{ km}$, where both the laminar flame speeds and widths are log–log fits as functions of density for a 50/50 C–O fuel mixture from Chamulak et al. (2007) with $\text{Pr} = 10^{-5}$, where Pr is the Prandtl number that describes the ratio of kinematic viscosity to thermal diffusivity. The blue line shows the limiting behavior with $\Xi_\Delta = 1 + u'_\Delta/s_l^0$, while the black line is the fitted laminar flame speed. These estimates were calculated with $\Delta = 16 \text{ km}$, which is approximately the length scale associated with the turbulence measure for $h = 1$ in a 4 km resolution simulation.

This scaling, however, does not extend to infinitely low s_l^0 . At some stage Ξ is as high as it can be given the finite width of the flame and the volume it represents, and the Damköhler relation is no longer followed. As a result, as s_l^0 decreases and δ_l^0 increases, $s_{l\Delta}$ should fall off at low densities. The cut-off to $s_{l\Delta}$ that has typically been used in previous models (Schmidt et al. 2006b; Townsley et al. 2007) is given by the vertical dashed line in Figure 4. This line corresponds to estimates of the density at which combustion in a degenerate WD transitions from the flamelet regime to the “distributed burning” or “broken reaction zone” regime. This estimate is typically derived from the condition that $\ell_G \lesssim \delta_l^0$, where ℓ_G is the Gibson scale that describes the length scale at which the turbulent eddies are burned by the flame in less than an eddy turnover time. If ℓ_G drops below δ_l^0 , turbulent eddies can turnover inside the flame structure and contribute to the transport of mass and heat. If this transition occurs, the flame is no longer a well-defined concept, and the assumptions used in the construction of the models for turbulent combustion are no longer valid.

The general concept explored by both **CVDP** and **CMV** based on earlier work by Meneveau & Poinso (1991) is to integrate the wrinkling over many scales (through the cascade) in order to consider separately the contributions from above and below the approximate LES smoothing scale Δ . At the heart of this method is the consideration of single-scale flame–vortex interactions. Using DNS of single flame–vortex interactions, **CVDP** investigate the efficiency of the vortex to wrinkle the flame when the ratio of the vortex size (r) to laminar flame width and ratio of the vortex velocity (v') to the laminar flame speed varies. An SGS model is constructed by calculating the effective strain rate on the flame by integrating the efficiency of single flame–vortex interactions (computed from DNS) through the unresolved inertial range of the turbulent cascade. This introduces two important questions: how does the contribution to wrinkling depend on scale? and what is the appropriate inner cutoff scale under various conditions? These will be answered in different ways by the models discussed.

5.2. Power-Law Flame Wrinkling Model

CMV focus on modeling the wrinkling of the unresolved physical flame. They consider a flame that is fractal in nature, with an inner scale determined by the characteristics of the turbulence and flame. They also consider the possibility that the fractal dimension could depend on other local properties, but we do not include this part of their analysis (Charlette et al. 2002b). **CMV** postulate that the inner length scale is the inverse mean curvature of the flame, which they solve for directly using the flame surface density balance equation and the hypothesis that flame surface destruction and production are in equilibrium on unresolved scales. This construction requires only grid-scale quantities to be known, an advantage over the methods discussed by **CVDP** (see Section 5.3). The only stipulation to recover Damköhler scaling is that, in this limit, the fractal dimension of the flame should be $D = 7/3$.

CMV obtain their power-law flame wrinkling model from the postulate that the wrinkling factor is a simple power function involving the dimensionless ratio of the smoothing scale Δ to the inner cutoff scale of the flame structure η_c . This is expressed by the wrinkling factor given in **CMV**, Equation (3):

$$\Xi_\Delta = \left(1 + \frac{\Delta}{\eta_c}\right)^\gamma, \quad (18)$$

where then $s_{l\Delta} = \Xi_\Delta s_l^0$, and γ is not necessarily constant. If γ is independent of scale and restricted to $0 < \gamma < 1$, the fractal model is recovered where the fractal dimension $D = \gamma + 2$. In the limit of strong turbulence, $\gamma = 1/3$ in order to recover Damköhler scaling as shown in Figure 4. The inner cut-off scale η_c is estimated to be the inverse mean curvature of the flame ($|\langle \nabla \cdot \mathbf{n} \rangle_s|^{-1}$). This is then obtained by assuming equilibrium between subgrid flame surface creation (strain) due to wrinkling by the turbulence and flame surface destruction by flame surface propagation and diffusion. This gives **CMV**, Equation (10):

$$\eta_c^{-1} = |\langle \nabla \cdot \mathbf{n} \rangle_s| = \Delta^{-1} \frac{u'_\Delta}{s_l^0} \Gamma \left(\frac{\Delta}{\delta_l^0}, \frac{u'_\Delta}{s_l^0}, \text{Re}_\Delta \right), \quad (19)$$

where $\Gamma(\cdot)$ is an efficiency function which takes into account the net straining effect of all relevant turbulent scales smaller than Δ , and is derived by integrating over the single-vortex efficiency function, C (**CVDP**), and a turbulence spectrum (see below). The inverse mean curvature is related to the Gibson scale, although it is not immediately obvious. See the discussion of the scaling in various regimes in **CMV**.

CMV prevent the unphysical result, $\eta_c < \delta_l^0$, with

$$\eta_c = \max(|\langle \nabla \cdot \mathbf{n} \rangle_s|^{-1}, \delta_l^0). \quad (20)$$

This limiting behavior provides a natural and physical way to quench flames. Even for a space-filling flame with $\gamma = 1$, there is a finite amount of flame surface that can physically exist on unresolved scales for a finite-width flame. Models currently in use, including Khokhlov (1995) and **SNHR**, do not consider this effect, which may be important for combustion in SNe Ia for the density range 10^7 – 10^8 g cm $^{-3}$. Instead, these approaches typically set $s_{l\Delta} = 0$ for $\rho < 10^7$ g cm $^{-3}$, where ρ is the fuel density.

The spectral efficiency function Γ utilizes an efficiency function C modified from **CVDP**, such that vortices with speed $v' < s_l^0/2$ do not wrinkle the flame. Additionally, the integration over length scales is performed in k -space in **CMV**, Equation (13):

$$\left(\Gamma \frac{u'_\Delta}{\Delta}\right)^2 = \int_{\pi/\Delta}^{\infty} [C(k)]^2 k^2 E_{11}(k) dk, \quad (21)$$

where $E_{11}(k)$ is the one-dimensional energy spectrum describing homogeneous, isotropic turbulence in the direction of the wavenumber k , given in **CMV**, Equation (16). Because $E_{11}(k)$ depends on Pr , we re-evaluate the numerical integral for $\text{Pr} = 10^{-5}$ to compare with fitting functions provided by **CMV** in Figure 5. Numerical integrals are computed using **CMV**, Equations (18)–(21) and Equation (26) with subroutine `dqag` from the publicly available SLATEC library. Because the integrand is non-oscillatory, smooth and tends toward zero exponentially as the argument goes to infinity, we choose an upper bound to the integral such that the integrand evaluates to a number less than 10^{-10} . This criterion is sufficiently small as compared to the integrand evaluated at the lower bound. A good initial guess at the upper bound is given by 10^3 multiplied by **CMV**, Equation (26), which approximates the maximum of the integrand. We evaluate Γ with an error tolerance of 0.1% and found that a Gauss–Kronrod pair with 15–31 points provides consistent results for a wide range of parameter space. We also use the fitting function for Γ given in **CMV**, Equations (30)–(34) in a range outside that explored by **CMV**. We compare numerically integrated values (points) to the fit (thin dashed lines) for

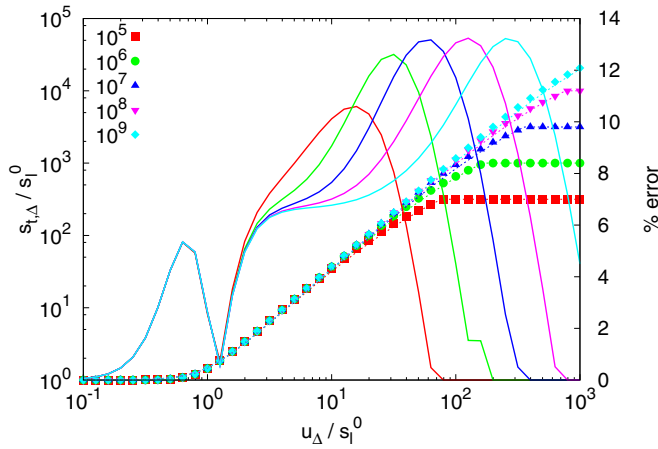


Figure 5. Enhancement to the laminar flame speed for $\text{Pr} = 10^{-5}$ is shown as a function of the ratio of the turbulent intensity at the scale Δ to the laminar flame speed (u'_Δ/s_1^0) on the x -axis and the ratio of Δ to the laminar flame width (Δ/δ_1^0) with different colors. The numerically integrated values are shown as points while the fit values are shown as thin dashed lines. The percent error between the fit and the numerically integrated result are shown as thick solid lines with the error given on the second y -axis. The range of values chosen represents the range of expected values for a moderate resolution SN Ia simulation. The fit-errors are all $\lesssim 10\%$.

(A color version of this figure is available in the online journal.)

$\Delta/\delta_1^0 = 10^5 - 10^9$ and a range of u'_Δ/s_1^0 up to 10^3 . The associated percent errors are provided as thick lines in Figure 5.

For comparison, results from the power-law flame wrinkling model with $\gamma = 1/3$ corresponding to the limiting Damköhler scaling behavior are shown in magenta in Figure 4. Given the arguments by CMV that $\Xi^1 \approx 1$ and the ambiguities associated with choosing a cut-off scale δ_l^c in the models derived below from CVDP, we choose to implement the power-law flame wrinkling model. The power-law flame wrinkling model provides a more natural mechanism to quench turbulent flames rather than supplying an ad hoc prescription as in other models (Schmidt et al. 2006a; Townsley et al. 2007). Additionally, the implementation requires only grid-scale quantities, which are computationally accessible.

5.3. Other Models Considered: A Priori Cutoffs

CVDP specifically investigate a model applicable to artificially thickened flames. In order to achieve a thickened flame resolvable by the computational domain, the thermal and molecular diffusivities are enhanced by a thickening factor F , while the reaction rate is reduced by F . However, by increasing the diffusivity, the thickened flame is less responsive to strain on the flame front due to turbulence. Thus, while the flame is resolved on the domain, the interaction with turbulence is affected. Because the utilization of artificially thickened flames greatly reduces computational costs while capturing many of the inherent phenomena associated with combustion, CVDP attempt to account for inefficient wrinkling of the artificially thickened flame by resolved turbulence. Thus the formalism tries to consider the context in which both the artificial and real flames exist, and correct the former to the latter. Since it is posed as a relative correction, rather than an absolute calculation of surface area, the wrinkling factors must be normalized to reproduce some limiting behavior, taken to be Damköhler scaling ($s_t \propto u'$). Posed in this way, the resulting normalization requires integral scale quantities to be known, such as the integral scale (ℓ_t), turbulent intensity (u'), and Reynolds number (Re). This also

creates the situation where an a priori choice must be made for the appropriate small-scale cut-off under which Damköhler scaling is recovered.

In CVDP, the enhancement to the laminar flame speed is given by the ratio of the wrinkling factor for the thin flame to the wrinkling factor for the thick flame, $E = \Xi^0/\Xi^1$. Here, the superscript 0 refers to the real physical “thin” flame, and the superscript 1 refers to the model “thick” flame. Here now $s_{t\Delta} = E s_1^0$, since $\Xi^1 \neq 1$. The wrinkling factor is given by equating subgrid flame surface production from turbulent wrinkling to subgrid flame surface destruction by propagation and diffusion from the subgrid flame surface density balance equation in CVDP, Equation (18):

$$\Xi \approx 1 + \alpha \frac{\Delta}{s_1^0} \langle a_T \rangle_s, \quad (22)$$

where α is a model constant, Δ is the length scale associated with the turbulence operator, and $\langle a_T \rangle_s$ is the effective strain rate averaged over the flame surface on SGSs. The effective strain rate is given by CVDP, Equation (24) calculated by integrating turbulent motions over the inertial range by an efficiency function derived from DNS calculations:

$$\langle a_T \rangle_s = \frac{c_{ms}}{\ln(2)} \int_{\text{scales}} C \left(\frac{r}{\delta_l^c}, \frac{v'}{s_1^0} \right) \frac{v'}{r} d \left[\ln \left(\frac{\ell_t}{r} \right) \right], \quad (23)$$

$$= \Gamma \left(\frac{\Delta}{\delta_l^c}, \frac{u'_\Delta}{s_1^0} \right) \frac{u'_\Delta}{\Delta} \quad (24)$$

where c_{ms} is a constant determined from DNS calculations (Yeung et al. 1990) and s_1^0 refers to the unstrained laminar flame speed (superscript 0 referring to unstrained). Note that the efficiency function and the integration differ slightly from CMV. The result, Γ , of performing this integration with the DNS-derived efficiency function, C , is given by CVDP, Equation (30). This leaves α to be determined. In order to evaluate the limiting case of Damköhler scaling ($\Xi \approx 1 + \beta u'/s_1^0$), a simple Heaviside efficiency function is introduced for C with a cut-off scale δ_l^c , such that $C = 0$ for $r < \delta_l^c$ and $C = 1$ for $r > \delta_l^c$. In this case, the integral can be solved analytically with the caveat that $\delta_l^c \geq \eta_k$:

$$\alpha = \beta \frac{2 \ln(2)}{3 c_{ms}} \left[\left(\frac{\ell_t}{\delta_l^c} \right)^{2/3} - 1 \right]^{-1}, \quad (25)$$

where β is a model constant of order unity. We describe two procedures to calculate α that lead to two different models.

5.3.1. Full Inertial Range Model

CVDP argue Damköhler scaling is achieved only when the flame front is wrinkled by *all* turbulent motions in the inertial range, from η_k to ℓ_t . This hypothesis defines the model we call the “Full Inertial Range” (FIR) model. For astrophysical flames, typically $\eta_k \ll \delta_1^0$, which means that α will be relatively small, and the model will not predict much enhancement.

CVDP let $\delta_l^c = \eta_k$ to evaluate α in Equation (25). When $\delta_l^c = \eta_k$, $(\ell_t/\delta_l^c)^{2/3} = \text{Re}^{1/2}$. Here, the evaluation of Re becomes important, where $\text{Re} = \ell_t u'/\nu$, and integral scale quantities are necessary. We prefer to write Re_Δ for scale Δ in terms of the ratios u'_Δ/s_1^0 and Δ/δ_1^0

$$\text{Re}_\Delta = \frac{u'_\Delta}{s_1^0} \frac{\Delta}{\delta_1^0} \frac{s_1^0 \delta_1^0}{\nu} = \frac{u'_\Delta}{s_1^0} \frac{\Delta}{\delta_1^0} \text{Pr}^{-1}, \quad (26)$$

where $s_1^0 \approx \sqrt{\kappa/\tau_r}$ and $\delta_1^0 \approx \sqrt{\kappa\tau_r}$, such that $s_1^0\delta_1^0 = \kappa$, where κ is the thermal diffusion coefficient and τ_r is the reaction timescale. Then, $\text{Pr} = \nu/\kappa$. Here, δ_1^0 refers to the physical laminar flame width; whereas, δ_1^1 will refer to the model flame width. Re at the integral scale can be evaluated with $\Delta = \ell_t$. For terrestrial flames, $\text{Pr} \sim 1$ with CVDP choosing $\text{Pr} = 1/4$; however, astrophysical flames characteristic for a degenerate WD have Pr as low as 10^{-5} (Nandkumar & Pethick 1984; Niemeyer & Kerstein 1997; Kerstein 2001). In our simulations, integral scale quantities are not easily accessible and it is useful to solve for α at the scale Δ such that

$$\Xi_\Delta = 1 + \alpha \frac{\Delta}{s_1^0} \langle a_T \rangle_s = 1 + \beta \frac{u'_\Delta}{s_1^0}. \quad (27)$$

This means that the turbulent flame speed at the scale Δ obeys Damköhler scaling when all turbulent motions of size r with $\delta_l^c < r < \Delta$ wrinkle the flame with full efficiency. For the implementation in which $\delta_l^c = \eta_k$, we obtain

$$\alpha_{\text{FIR}} = \beta \frac{2 \ln(2)}{3c_{ms}} \text{Re}_\Delta^{-1/2}. \quad (28)$$

For low-Pr flames, we never actually recover $\Xi_\Delta = 1 + \beta u'_\Delta/s_1^0$ because $\eta_k < \delta_1^0$. As seen from the red curve in Figure 4, $s_{t\Delta}$ is never much more than s_1^0 , which does not meet our expectations for the behavior of the turbulent flame speed in these circumstances. For these reasons, we consider another normalization to solve for α .

5.3.2. Flame Width Cutoff

Instead of only allowing Damköhler scaling when the flame is wrinkled by the full inertial range, we allow Damköhler scaling when the flame is influenced by all turbulent eddies ranging from Δ to the flame scale, letting $\delta_l^c = \delta_1^0$. This hypothesis defines the model we call the ‘‘Flame Width Cutoff’’ model. With $\Delta/\delta_1^0 \gg 1$, the evaluation of α becomes

$$\alpha_{\text{Flame Width Cutoff}} = \beta \frac{2 \ln(2)}{3c_{ms}} \left(\frac{\Delta}{\delta_1^0} \right)^{-2/3}. \quad (29)$$

The resulting $s_{t\Delta}$ is shown by the green line in Figure 4, and provides a reasonable approximation of the expected behavior. The apparent physical underpinnings for this are, however somewhat suspect. We have made the assumption that Damköhler scaling holds whenever the turbulence cascade reaches the flame width. This creates the unphysical result that when δ_l^0 starts to become large, the model assumes that the resolved flame will capture the Damköhler scaling, and the enhancement falls off. This is therefore not a physically consistent model, despite having the expected behavior, and leads us again to prefer the construction of CMV.

6. VERIFICATION

We present two formal verification (Calder et al. 2002) tests of our TFI model as a whole. The whole model includes the turbulence measurement operator described in Section 4, the TFI prescriptions developed from the power-law flame wrinkling model of CMV, as presented in Section 5.2, and a ADR scheme for propagating the reaction front, described in previous work (Vladimirova et al. 2006; Townsley et al. 2007). We wish to verify by numerical tests that the TFI model produces sensible

results in two regimes: negligible turbulence and moderate-strength freely decaying homogeneous turbulence. These are the most important regimes for the early part of the SN Ia. We constrain ourselves to the type of turbulence considered in construction of the model, leaving more complex turbulence fields to future work.

6.1. TFI Channel Test

It is important to develop flow configurations that are simultaneously numerically tractable and provide meaningful verification of TFI techniques. Those performed in the astrophysical literature so far have used flames in a fixed-size box of stirred turbulence (SNH; see also Schmidt 2004), a flame propagating up a vertical channel with self-created turbulence due to the RTI (Khokhlov 1993, 1995; Zhang et al. 2007; D. M. Townsley et al. 2008, private communication), and a flame propagating along a channel into a driven turbulent velocity field Aspden et al. (2008). Motivated by CMV, here we develop and utilize a configuration based on a flame propagating along a channel into a field of decaying turbulence. Our basic configuration is shown in Figure 2, in which a flame is allowed to propagate longitudinally along a (laterally periodic) channel against the prevailing flow. A turbulent field, obtained from a stirred turbulence simulation, is placed immediately ahead of the flame and allowed to decay as the flame propagates into it.

In order to test our implementation of the power-law flame wrinkling SGS TFI, we use a simple one-stage model flame described in Vladimirova et al. (2006); Townsley et al. (2007). The model flame is described by a reaction progress variable, ϕ , that is evolved by an advection-reaction-diffusion equation where the reaction and diffusion terms are chosen to yield a specified front propagation speed and model flame width (Khokhlov 1995). The use of a one-stage burner with a known energy release results in an analytic solution to the Rankine–Hugoniot jump conditions across the flame used to set up the initial conditions. For our tests, our flame burns a 50/50 carbon–oxygen mixture by mass to 50/50 oxygen–magnesium, which is equivalent to the simplified prescription of the carbon burning stage in our three-stage flame model that is designed to capture the energetics in SNe Ia (Townsley et al. 2007). For simplicity, we specify constant laminar flame speed properties with a speed of 10 km s^{-1} and physical width of 10^{-3} cm .

The flame is initialized in the center of a box that is four times longer than it is wide using Cartesian coordinates with the model flame resolved using four zones propagating in the positive direction of the first dimension. Subsonic inflow and outflow boundary conditions motivated by Poinso & Veynante (2005) are imposed. A subsonic inflow boundary condition is used with an inflow velocity initially equal to the specified front propagation speed such that the model flame remains in the center of the box. The inflow velocity is allowed to vary for turbulent flows such that fuel is in-flowing at the burning rate

$$v_{\text{inflow}} = \frac{\dot{m}_b}{A_{\text{inflow}} \rho_{\text{fuel}}}, \quad (30)$$

where v_{inflow} is the inflow velocity defined to be positive in the $-x$ direction, \dot{m}_b is the burning rate and A_{inflow} is the cross-sectional area of the inlet. The burning rate is calculated from the change in mass of ash on the grid between time steps and the ash outflow rate

$$\dot{m}_b = \frac{m_{\text{ash}}^n - m_{\text{ash}}^{n-1}}{t^n - t^{n-1}} + \langle \rho v_{\text{outflow}} \rangle A_{\text{outflow}}, \quad (31)$$

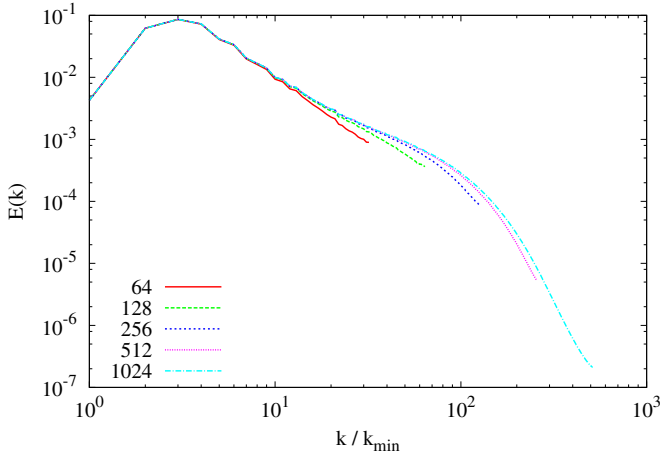


Figure 6. Normalized spectral energy content for smoothed velocity fields resulting from the 1024^3 -resolution turbulence run in Figure 3 as a function of wavenumber in units of $2\pi/L$.

(A color version of this figure is available in the online journal.)

where v_{outflow} is the outflow velocity defined to be positive in the $-x$ direction, A_{outflow} is the cross-sectional area of the outlet, $m_{\text{ash}} = \int \phi \rho dV$ and t^n denotes the n -th time step. A static-pressure subsonic outflow boundary condition is imposed that conserves mass and energy through the boundary using the steady-state Euler equations and divergence theorem assuming zero-gradient velocities in orthogonal directions. Because the steady-state continuity equation is satisfied, ρv_{outflow} is constant across the boundary allowing an average, $\langle \rho v_{\text{outflow}} \rangle$, over the interior boundary cells. A static-pressure outflow reflects sound waves back into the computational domain, which are necessary to stabilize the flow. The inflow temperature is strictly maintained, while the inflow velocities are allowed to vary to ensure acoustic reflections back into the computational domain are dampened. If perfectly reflecting boundary conditions are used on both the outflow and inflow, sound waves never leave the computational domain. Periodic boundary conditions are imposed in the second and third dimensions.

Our verification tests include simulating a laminar flame in a channel with varying resolutions from 64×64 to 256×256 zones in cross-sectional resolution. Cells are cubic and the total simulated domain is twice as long in the longitudinal direction as it is in the transverse direction. While these resolutions are possibly too low to capture a true inertial range, they are similar to conditions in the SN that are challenging for the same reason. Because the initial profile given for the reaction progress variable, ϕ , is not equal to the true steady state profile, it takes a few flame self-crossing times, $\tau_{\text{flame}} = \delta_1^1/s_1^0$, to obtain a steady state solution. Firstly, we verify that for perfectly laminar flow, the TFI model recovers the laminar flame speed as expected. Afterward, we restart the simulation by superimposing a turbulence field with a specified turbulent intensity in the fuel. The turbulence field used is the same as the 1024^3 resolution run used to calibrate the constant c_2 in Section 4 with the velocities normalized by v_{rms} . In addition, velocities are smoothed via direct averaging to obtain lower-resolution turbulent velocity fields. This procedure allows a direct comparison of the TFI model as the inertial range of the turbulent cascade is better resolved. The power spectra of the smoothed velocity fields is provided in Figure 6. These simulations are computed for various resolutions to verify that the combined effects of resolved and unresolved TFI result in a

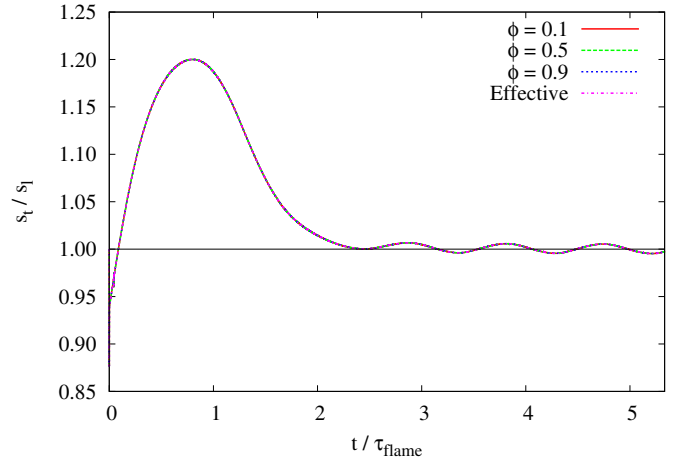


Figure 7. Ratio of the front propagation speed to input speed of the iso-contours of the reaction progress variable for $\phi = \{0.1, 0.5, 0.9\}$ (red, green, and blue lines, respectively) as well as the turbulent flame speed (magenta) are compared. The initial flow is computed by solving the Rankine–Hugoniot jump conditions in the reference frame of the flame such that the flame remains in the center of the domain (Vladimirova et al. 2006). The small oscillations in the estimated flame speed are discussed in Townsley et al. (2007).

(A color version of this figure is available in the online journal.)

consistent overall turbulent flame speed independent of the grid resolution.

In each of these tests, the flame speed is computed with

$$s_A = \frac{\dot{m}_b}{A \langle \rho_{\text{fuel}} \rangle}, \quad (32)$$

where s_A is the flame speed computed from using area A , which is the surface area of an iso-contour of the reaction progress variable to compute the front-propagation speed or the cross-sectional area of the channel to compute the turbulent flame speed. In the case of an iso-contour, the surface area is computed using the marching cubes algorithm. We estimate the fuel density by assuming a low Mach number isobaric burn and solving for $\rho(\phi = 0)$ from (Vladimirova et al. 2006)

$$e(p, \rho) + \frac{p}{\rho} + q\phi = \text{const} \quad (33)$$

$$p = \text{const}, \quad (34)$$

where q is the total energy released through the burn, p is the pressure, and e is the specific internal energy determined from the equation of state. The averaging procedure to obtain $\langle \rho_{\text{fuel}} \rangle$ is performed on densities just ahead of the flame with $10^{-6} < \phi < 5 \times 10^{-2}$.

6.2. Recovering the Laminar Flame Speed

We test the implementation of u'_Δ in Equation (8) and the power-law flame wrinkling SGS TFI model in the limit of $u'_\Delta/s_1^0 \rightarrow 0$. In this limit, the turbulence operator is constructed to ignore the expansion of material due to laminar flame propagation and $u'_\Delta = 0$ should be observed. In addition, the TFI model should calculate the enhancement $\Xi_\Delta = 1$ such that $s_{\text{td}} = s_1^0$. For this test, we fix the inflow velocity equal to the input front-propagation speed and do not allow it to vary. In Figure 7, we plot the ratios of the front-propagation speeds to the input speed of the iso-contours of the reaction progress variable for $\phi = \{0.1, 0.5, 0.9\}$ as well as the turbulent flame speed

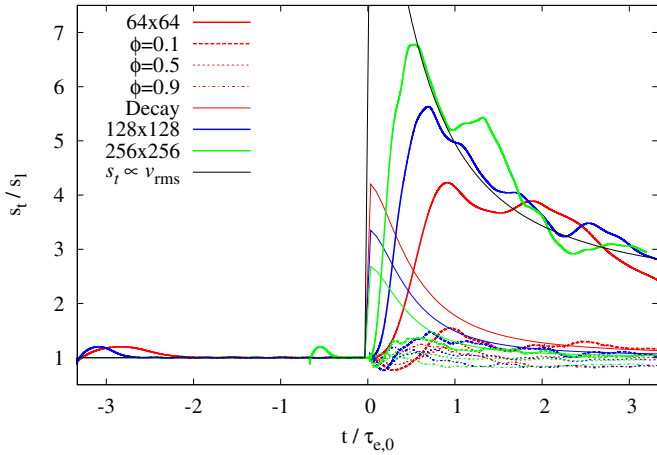


Figure 8. Ratio of the front propagation speed to input speed of the iso-contours of the reaction progress variable for $\phi = \{0.1, 0.5, 0.9\}$ (dashed, dotted, and dot-dashed lines, respectively) as well as the turbulent flame speed (thick solid lines) are compared to the estimated turbulent flame speed from the decaying turbulence (thin solid lines). The thin black line provides the Damköhler scaling relation for decaying turbulence. Cross-sectional resolutions of 64×64 (red), 128×128 (blue), and 256×256 (green) are compared by super-imposing a turbulent velocity field in the fuel with $v_{\text{rms}} = 100 \text{ km s}^{-1}$. The flow is not driven, so the turbulence field decays from numerical dissipation at the grid scale and the estimated front-propagation speeds of iso-contours of ϕ return to the input front-propagation speed. An SGS model is not used for these calculations, and the solution does not converge with resolution.

(A color version of this figure is available in the online journal.)

compared. All estimated flame speeds are perfectly consistent with one another indicating that the area of each iso-contour and the cross-sectional area of the channel are all equivalent. The initial adjustment and subsequent oscillation of the $\phi(x)$ profile is related to the flame self-crossing time $\tau_{\text{flame}} = \delta_l^1/s$, which is described in detail in Townsley et al. (2007). This shows that the turbulence operator indeed measures $u'_\Delta = 0$ and that the resulting flame speed is equivalent to the laminar (or input) flame speed. The Landau–Darrieus instability is not observed because the initial profiles are sufficiently flat that it does not grow significantly in this short timeframe.

6.3. Convergence Study

By increasing the resolution of the computational domain, more of the turbulent cascade is resolved and wrinkling of the flame is captured directly. By virtue of using a SGS model to account for unresolved turbulence, we expect that combined effects of unresolved and resolved turbulence should result in the same global turbulent flame speed independent of the resolution chosen. Note that strict convergence, for which an order can be defined, is not expected. Higher resolutions have both a smaller dissipation scale as well as a thinner reaction front, thus posing different physical problems. Instead we look for consistency among resolutions.

Figures 8 and 9 show the results of simulations with 64^2 , 128^2 , and 256^2 cells resolving the plane orthogonal to the direction of propagation. Figure 8 shows results if a TFI model is not used, and Figure 9 shows results using the TFI model implemented in this work. Initially, the turbulent velocity field is scaled to $v_{\text{rms}} = 100 \text{ km s}^{-1}$, giving a Gibson scale of 500 cm, or $1/3000$ of L . The global turbulent flame speeds computed from the fuel consumption rates are given by the thick solid lines, which are consistent with one another when the TFI model is included. When no TFI model is included, the burning rates

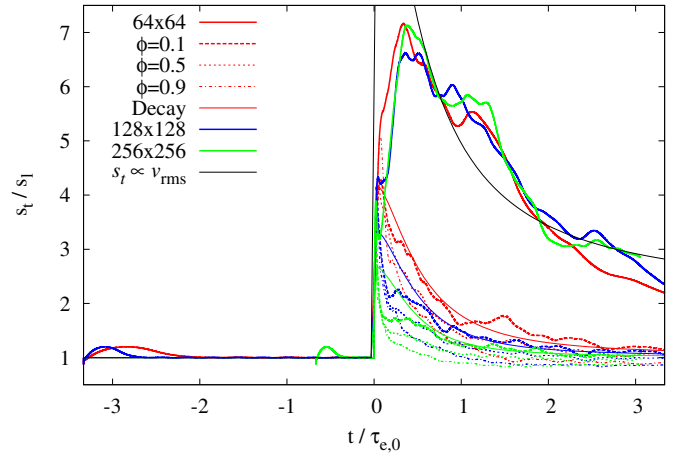


Figure 9. Same as Figure 8, except that the power-law flame wrinkling model is used and convergence with resolution is achieved.

(A color version of this figure is available in the online journal.)

obtained depend strongly on resolution. If the burning rates with the TFI model are correct, then the 256 resolution case without the TFI model is near convergence for the gross burning rate. Interpreting this result naively, neglecting subgrid TFI is not too bad when $\Delta_x \lesssim 10\lambda_G$. By contrast even the 64 cell resolution case with the TFI model included is already converged. This is consistent with the idea that the TFI model should give accurate results regardless of Δ_x/λ_G as long as there is enough resolution for a turbulence cascade.

The front-propagation speed based on areas of iso-surfaces of the reaction progress variable $\phi = \{0.1, 0.5, 0.9\}$ are given as dashed, dotted, and dot-dashed lines with the $\phi = 0.1$ line thickened to illustrate that with increased resolution, the unresolved portion of the inertial range contributes less to the global turbulent flame speed. From the case without a TFI model, it appears that the disruption of the reaction-diffusion front, which might appear as significant differences among the iso-surface areas, does not occur even though the lower resolution cases are clearly under-representing the total flame propagation. This is likely due to the proximity of the dissipation scale to the flame width, as both are related to the grid resolution.

Because the turbulence field is not driven in the fuel ahead of the flame, the turbulent velocity decays relatively quickly. In a separate calculation, the 256^3 -resolution run from Section 4 was restarted with no stirring to characterize the decaying turbulence field. The decaying power spectra maintain a Kolmogorov spectrum, while v_{rms} is described by

$$v_{\text{rms,decay}}(t) = e^{-t/\tau_e(t)}, \quad (35)$$

where $\tau_e(t) = A * t + B + C/t$ is the eddy turn-over timescale. As the velocity decays, the eddy turn-over timescale increases. The constants A , B , and C were determined using least-squares fits with $A = 0.4353\tau_{e,0}$, $B = 0.4454\tau_{e,0}$, and $C = 0.1973\tau_{e,0}$. This fit is consistent with the well-known result that $\langle u'^2 \rangle \propto t^{-1.3}$ for decaying turbulence after $\approx \tau_{e,0}$, but also accurately captures the decay for $t < \tau_{e,0}$. An eddy turn-over time is approximated by $\tau_{e,0} = L/v_{\text{rms}}$ where $L = 15 \text{ km}$. Therefore, an estimate of the turbulent velocity at a particular scale is provided by

$$u'_\Delta(t) = v_{\text{rms,decay}}(t) \left(\frac{\Delta}{L} \right)^{1/3}. \quad (36)$$

An estimated turbulent flame speed at scale Δ is calculated analytically using the TFI model and provided for comparison

in Figures 8 and 9 as thin lines colored corresponding to the simulation. The expected result from Damköhler scaling ($s_t \propto u'$) at scale L is given by the thin black line in each figure. This estimate reasonably predicts the behavior of the flame speed after some delay time that appears to be related to τ_{flame} . The reaction-diffusion front requires $1-2\tau_{\text{flame}}$ to equilibrate to the flow around it. Without the utilization of a TFI model, τ_{flame} is resolution-dependent (see Figure 8). When a TFI model is used, the front propagation speed is increased such that τ_{flame} is resolution-independent, resulting in the better convergence seen in Figure 9.

While we have shown convergence over a factor of 4 in resolution, this result does not preclude the possibility that the TFI model may not accurately represent the TFI over a broader range of scales such as those being modeled in SN Ia simulations. To extend our analysis to larger computational domains is prohibitively expensive, and we leave this concern to future work.

7. FUTURE CONSIDERATIONS

In order to improve upon this model, DNS calculations of single vortex-flame interactions should be computed for low-Pr, high-Le flames to verify the efficiency function for astrophysical flames. Unfortunately, these calculations are expensive and outside the scope of the present study. Zingale et al. (2001) provided preliminary results of exactly this calculation; however, a more comprehensive and complete analysis is required.

Future calculations should also consider flame curvature and stretch effects, especially for high-Le flames. Currently, this model assumes CMV, Equation (6),

$$-\langle w \nabla \cdot \mathbf{n} \rangle_s \approx s_1^0 |\langle \nabla \cdot \mathbf{n} \rangle_s|, \quad (37)$$

when $\eta_c > \delta_1^0$, to describe the destruction of flame surface density due to the laminar flame propagation. Here, w is the flame front displacement speed, $|\langle \nabla \cdot \mathbf{n} \rangle_s|$ is the mean curvature of the flame, and s_1^0 is the unstrained laminar flame speed. However, if one considers thermodiffusive effects for flames with arbitrary Le, then

$$-w = s_1^0 \left[1 + \left(\frac{1}{\text{Le}} - 1 \right) \frac{\text{Ze}}{2} \nabla \cdot \mathbf{n} \right], \quad (38)$$

to linear order in curvature (see, e.g., Dursi et al. 2003), where Ze is the Zeldovich number that describes the strength of the temperature sensitivity of the driving reaction. For $\text{Le} \approx 1$, Equation (37) is appropriate; however, for $\text{Le} \neq 1$, as in thermonuclear flames, it is not a good approximation.

Still, one could assume that regions of positive curvature never completely quench the flame (i.e., $w > 0$ always), and

$$-\langle w \nabla \cdot \mathbf{n} \rangle_s \approx s_1^0 \left[|\langle \nabla \cdot \mathbf{n} \rangle_s| + \left(\frac{1}{\text{Le}} - 1 \right) \frac{\text{Ze}}{2} \langle (\nabla \cdot \mathbf{n})^2 \rangle_s \right]. \quad (39)$$

In this case, it is possible for the mean curvature to be zero, yet for the average front propagation speed to be significantly different from s_1^0 . In this case, the inner cutoff scale η_c that describes a fractal-like flame would be better defined by the root-mean-squared flame surface curvature. Of course, the relation between $\langle \nabla \cdot \mathbf{n} \rangle_s$ and $\langle (\nabla \cdot \mathbf{n})^2 \rangle_s$ would still need to be established, and would likely depend on the net strain rate and/or the Damköhler number to indicate how easily the flame is packed by turbulence.

While the inverse mean curvature of the flame is prevented from becoming smaller than the laminar flame width artificially, more physical constraints may be constructed by considering flame merging and quenching processes. As the mean curvature increases, higher-order flame surface density destruction terms due to merging may become important (Meneveau & Poinso 1991). The inclusion of merging and quenching processes into the model may naturally prevent the mean curvature of the flame from becoming too large and will provide a smooth transition from moderate mean curvature to strong mean curvature. Recent calculations by Poludnenko & Oran (2010, 2011) indicate that the transition to “distributed burning” or “broken reaction zones” require higher turbulent intensities than previously thought. This result implies that the flame remains a well-defined concept into the “thin reaction zone” and that model improvements may extend the range of validity to higher-intensity turbulence.

As a possibly essential addition, the effect of unresolved RT modes should be self-consistently incorporated into the SGS TFI model. This instability could be incorporated into the energy function $E(k)$ using an appropriate efficiency function with a critical scale being the so-called “fire-polishing” scale ℓ_{fp} . Ciaraldi-Schoolmann et al. (2009) has shown that the turbulent energy spectrum for $\mathbf{k} \parallel \mathbf{g}$ follows that expected from RT scaling, while for $\mathbf{k} \perp \mathbf{g}$ the energy spectrum follows homogeneous and isotropic turbulence. We plan to include the effect of increased flame surface due to RTI in future modeling efforts. Currently, we instead choose the turbulent flame speed based on the dominant effect such that

$$s_t = \max(s_{\text{TFI}}, s_{\text{RT}}), \quad (40)$$

where s_{TFI} is the turbulent flame speed estimated from the TFI model described in this work and s_{RT} is the turbulent flame speed estimated from RTI described in Khokhlov (1995) and Townsley et al. (2007). However, we still prevent s_t from increasing beyond the limit $s_1^0(1 + \Delta/\delta_1^0)^\gamma$, which provides a natural quenching process as burning progresses toward lower densities (see Figure 4).

8. COMPARING TFI MODELS IN SIMULATIONS OF SNe Ia

We perform three full-star, 3D simulations of the deflagration phase of a centrally ignited SN using FLASH with the flame resolved at 4 km and the star at 16 km. One simulation is performed without an explicit TFI model, which only accounts buoyancy effects by setting the turbulent flame speed to

$$s_{\text{t}\Delta} = s_{\text{RT}} = 0.5\sqrt{Agm\Delta}, \quad (41)$$

where the Atwood number

$$A = \frac{\rho_f - \rho_a}{\rho_f + \rho_a} \quad (42)$$

describes the density change across the flame, g is the local gravitational acceleration, and m is a calibrated constant determined to be $m \sim 0.04-0.06$ (D. M. Townsley et al. 2008, private communication). We will call this implicit TFI model the buoyancy-compensation model. Two more simulations compare the relation between u'_Δ and $s_{\text{t}\Delta}$. One assumes that the TFI is scale invariant which follows the simple prescription described by Pocheau (1994) and utilized by Schmidt et al. (2006a) given as

$$s_{\text{t}\Delta} = \sqrt{s_1^{02} + C_t u'_\Delta{}^2}, \quad (43)$$

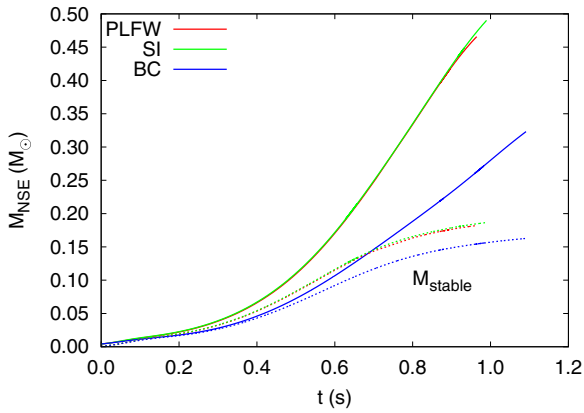


Figure 10. Yield of material in nuclear statistical equilibrium (NSE; solid lines) and an estimate of the yield of stable Fe-group elements (dotted lines) as a function of time for the power-law flame wrinkling (red), scale invariant (green), and buoyancy-compensation (blue) simulations. The simulations with explicit TFI (power-law flame wrinkling and scale invariant) show a larger production of material in NSE as well as stable isotopes during the deflagration phase; albeit, the difference in stable isotope production is smaller.

(A color version of this figure is available in the online journal.)

where C_t is a constant taken to be $4/3$, the same as that used in Schmidt et al. (2006b). We will call this model the scale invariant TFI model. The final simulation employs the power-law flame wrinkling model described in this work. Both of the latter simulations utilize the measure of turbulence described in Section 4. Note that the power-law flame wrinkling method was developed by CMV to not require any assumptions about integral scale quantities. The modeling is entirely based on measurement of turbulence characteristics on scales just above the grid scale.

All other aspects of the simulations are fixed relative to each other. We do not include an initial background turbulent velocity field as expected from Zingale et al. (2009); therefore, these tests serve to highlight the minimum difference expected from the choice of TFI model. We ignite a near-Chandrasekhar mass WD with a central density $\rho_c = 2.2 \times 10^9 \text{ g cm}^{-3}$ and central temperature $T_c = 7 \times 10^8 \text{ K}$. The initial WD is described in Jackson et al. (2010) as having an isentropic, carbon-depleted core with $X(^{12}\text{C}) = 0.4$ and an isothermal outer layer with $X(^{12}\text{C}) = 0.5$, where $X(^{12}\text{C})$ is the carbon mass fraction. We initialize the simulation by placing 844 spherical hot spots with radius $r = 10 \text{ km}$ randomly within the inner 150 km of the star. We follow the evolution until the flame reaches a density of $\sim 10^7 \text{ g cm}^{-3}$, at which point a detonation is expected in the deflagration-to-detonation paradigm.

As FLASH heavily utilizes adaptive mesh refinement capabilities, we perform two test simulations to quantify the effect the refinement criteria has on the development of turbulence. If burning generates significant turbulence ahead of the flame, then those regions should be resolved to the same scale as the flame to allow turbulence to develop without artificial numerical dissipation. One simulation is conducted with the inner 1024 km uniformly refined to capture any turbulence generated that may influence the flame propagation, while the other only refines energy-generating regions. Differences in the evolution of these two simulations are negligible, and we conclude that a uniformly refined region is not necessary for a non-turbulent initial condition.

While end-to-end simulations were not performed, qualitative differences may be discerned from the deflagration phases

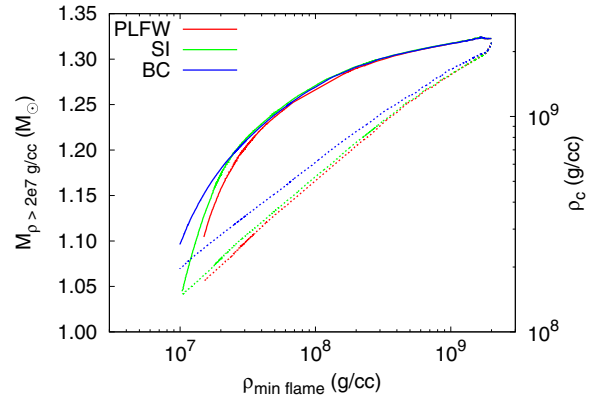


Figure 11. Amount of material at high density (solid lines; left y-axis) and central density (dotted lines; right y-axis) as a function of the minimum flame density for the power-law flame wrinkling (red), scale invariant (green), and buoyancy-compensation (blue) simulations. The material with $\rho > 2 \times 10^7 \text{ g cm}^{-3}$ is representative of the yield of Fe-group elements if a detonation were to be initiated at a particular instant in time (or a particular flame density). The simulations with explicit TFI (power-law flame wrinkling and scale invariant) show a faster expansion rate as evidenced by a steeper slope in the central density over the simulation with implicit TFI (buoyancy-compensation). This translates to nonlinear behavior in the estimate of final Fe-group yields with differences in the final yields diverging faster than the central densities as a function of the minimum flame density.

(A color version of this figure is available in the online journal.)

simulated. The largest differences occur between the explicit and implicit TFI treatments, with the implicit, buoyancy-driven treatment burning less fuel overall, and therefore expanding less rapidly. In addition, the simulation with implicit TFI produced fewer stable Fe-group elements. We conclude from these results that while using the implicit TFI model causes the star to expand less, the burning rate is even smaller, resulting in fewer stable Fe-group elements.

Figures 10 through 12 support this conclusion. Figure 10 compares the amount of material in nuclear statistical equilibrium (NSE) as well as the portion estimated to end up in the form of stable isotopes as a function of simulation time (see Jackson et al. (2010) for how this is estimated from the local Y_e). The explicit TFI models enhance burning in the turbulent regions dominated by the KH shear instability along the sides of the rising RT unstable plumes. This enhanced burning results in $\approx 0.2 M_\odot$ more material being processed to NSE as compared to the implicit TFI model. The difference in the amount of stable isotopes is less pronounced with a difference of $\approx 0.05 M_\odot$ between the models. While the final yield of Fe-group material is difficult to estimate from the deflagration phase alone, the final yield of stable Fe-group material should not differ very much from that produced during the deflagration. The separation in the curves that show the total NSE material and the stable portion occur at different times with the explicit TFI models separating around 0.2 s and the implicit TFI model around 0.4 s. While the implicit TFI model burns material at a slower rate, the expansion rate is also slower, allowing the processing of NSE material to occur longer at high density where weak processes are important. We expect the difference between explicit and implicit TFI models to be more stark with higher central density progenitor WDs. Figure 11 compares the expansion history of the WD in terms of the progression of the flame in density-space. We find this presentation most useful in assessing the outcome of a simulation in the context of the DDT paradigm as DDT is expected to occur when the flame reaches $\sim 10^7 \text{ g cm}^{-3}$. We plot two measures of the expansion as a function of the minimum

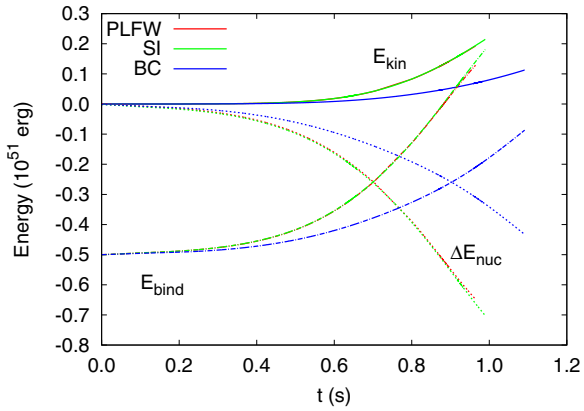


Figure 12. Energy budget as a function of time for the power-law flame wrinkling (red), scale invariant (green), and buoyancy-compensation (blue) simulations. The kinetic (solid lines), change in nuclear (dotted lines), and binding (dot-dashed lines) energies are compared. Nuclear energy is released as fuel with high rest-mass energy is processed to ash with low rest-mass energy. The released energy is converted into internal and kinetic energy, and serves to gravitationally unbind the star.

(A color version of this figure is available in the online journal.)

flame density: the amount of material with a density greater $2 \times 10^7 \text{ g cm}^{-3}$ on the left y-axis and the central density on the right y-axis. From previous studies (Townsend et al. 2009), we find that the amount of material with $\rho > 2 \times 10^7 \text{ g cm}^{-3}$ reasonably predicts the yield of NSE material if a detonation were to be triggered at that instant in time. From Figure 11, we expect $\sim 0.1 M_{\odot}$ difference in NSE yields between the buoyancy-compensation TFI model and the scale invariant TFI model, if DDT were to occur at $\rho_{\text{DDT}} = 10^7 \text{ g cm}^{-3}$. If DDT is delayed, the difference is expected to grow substantially since the expansion rates are very different. This figure demonstrates the only clear deviation between the two explicit TFI treatments, the power-law flame wrinkling and scale invariant models. The power-law flame wrinkling model appears to expand slightly more for the same flame progression that may result in a difference in the NSE yield of $\sim 0.05\text{--}0.1 M_{\odot}$ for $\rho_{\text{DDT}} = 10^7 \text{ g cm}^{-3}$, although if DDT were delayed the difference could be larger. Finally, Figure 12 shows the energy budget for the three different simulations, which supports the previously drawn conclusions. The implicit TFI model burns material at a slower rate, and releases less nuclear binding energy. This serves to delay the unbinding of the WD and results in a lower kinetic energy as compared to the explicit TFI model simulations. Additionally, note that both simulations with explicit TFI show the star unbinds during the deflagration phase, consistent with the centrally ignited, pure deflagration results of Röpke et al. (2007).

As simulations were only performed of the deflagration phase, only qualitative estimates of the final explosion outcome are provided. In general, it is clear that turbulence driven by KH instabilities in the wake of rising, RT unstable plumes serves to enhance burning in those regions than would otherwise be predicted by only considering buoyancy instabilities. The resulting increase in the burning rate leads to a different evolution of the flame and expansion of the star. We estimate that enhanced burning due to an explicit TFI treatment will result in $\gtrsim 10\%$ decrease in the total Fe-group yield, as well as $\gtrsim 30\%$ increase in the yield of stable Fe-group elements. In addition, the decrease in the efficiency of turbulence to wrinkle the flame at low density for the power-law flame wrinkling model compared to the scale invariant model may contribute to an additional

$\sim 10\%$ decrease in the total Fe-group yield. As a final note, the differences highlighted between the two explicit TFI models, the power-law flame wrinkling and scale invariant models, only highlight differences in how the turbulence measure is used, not how it is obtained. Simulations performed with the TFI model described by SNHR may show greater differences owing to the gradient-diffusion approximation for SGS turbulent transport.

9. CONCLUSIONS

We have implemented a power-law flame wrinkling TFI model based on CVDP and CMV. We calibrated a method used in FLASH to measure the turbulent velocity at the grid scale and have shown its validity over a range of calculations with increasing resolution. We compared and explored different implementation choices relevant for astrophysical flames ultimately deciding that a low-Pr extension of the CMV TFI model is most appropriate for SN Ia simulation. We provided two convincing test problems of the TFI model in FLASH for laminar and turbulent flows. Of most importance, we have shown that the global turbulent flame speed is consistent with increasing resolution where more of the inertial range is resolved on the computational domain. While this doesn't conclusively show that the model captures TFI for the full inertial range present in the explosion, the combined effects of the SGS TFI model with the resolved wrinkling of the model flame produce a consistent burning rate independent of resolution over a factor of 4. Additionally, we have shown that a laminar flame is recovered in the limiting case of laminar flow.

In order to understand how a power-law flame wrinkling model may effect the outcome of simulations of SN Ia, we compared full-star, 3D simulations of an SN Ia utilizing different treatments for the under-resolved TFI including one that considered only the effects of buoyancy on the turbulent flame as well as two others that additionally considered the directly measured turbulence local to the flame. The two latter simulations considered differences in the utilization of the same turbulence measure. We compared differences in the evolution of the deflagration phase of an SN Ia between the buoyancy-only model and the models that considered directly measured local turbulence. We demonstrated that the buoyancy-only model does not capture enhanced burning due to turbulence driven by the KH shear instability along the sides of rising, RT-unstable plumes. This deficiency in the buoyancy-only model leads to a reduced stable Fe-group yield and a larger overall Fe-group yield, which suggests an over-production of radioactive ^{56}Ni by $\gtrsim 0.2 M_{\odot}$ assuming DDT takes place when the flame reaches $\rho \approx 10^7 \text{ g cm}^{-3}$. If DDT occurs at lower densities, the difference is more pronounced. These estimates represent a lower-bound as the simulations performed did not include a turbulent background as expected from the slow smoldering of carbon during the process of thermonuclear runaway (Zingale et al. 2009). The turbulent background would only serve to enhance differences observed.

The demonstration of scale convergence of the SGS TFI model for homogeneous, isotropic, decaying turbulence will enable resolution studies of SN Ia simulations to determine whether the assumption of these turbulence properties on unresolved scales is valid. Failure to achieve convergence of the consumption rate in SNe Ia with resolution will indicate that additional unresolved physics important to the explosion process must be modeled. Such processes may be unresolved RT-unstable modes that contribute to flame surface growth or non-equilibrium turbulence.

This model limits the growth of flame surface based on the fact that the inverse mean curvature of the flame should not become smaller than the laminar flame width. This condition was shown to be similar to arguments that the turbulent flame should quench when $\ell_G < \delta_1^0$, although derived from the efficiency function describing the strain rate of individual eddies within the cascade. While this effect does not appear to be completely captured directly by the CVDP DNS calculations of flame–vortex interactions, it could be verified by future calculations.

Future calculations of SNe Ia will also benefit from the reliable measure of the turbulent velocity on unresolved scales in determining more realistic conditions for DDT. Our recent calculations (Townesley et al. 2009; Jackson et al. 2010; Krueger et al. 2010) determined DDT conditions simply by the requirement that the flame reach a particular density, ρ_{DDT} . This condition resulted in detonation ignitions at the “tops” of rising plumes where turbulence is expected to be relatively weak. A more appropriate DDT condition, viable in 3D simulations, is one based on the local turbulence intensity (e.g., Golombek & Niemeyer 2005). With such a more realistic DDT condition based on u'_{Δ} , detonations will likely ignite in the turbulent regions underneath plume caps.

Ideally, the TFI model would predict the DDT time and location during the explosion, thus removing a free parameter from the model. This would allow the explosion outcome to depend solely on the initial conditions of the WD and the distribution of the first flames. The accurate prediction of DDT is necessary to understand the range of properties of progenitor WDs that lead to realistic explosions, and how variations in those properties translate to variations in the explosion outcome.

The authors thank Alexei Poludnenko and Elaine Oran for useful discussions that contributed to this work. We also thank the anonymous referee for a careful reading of the manuscript and many suggestions that improved its accessibility. This work was supported in part by an award to A.P.J. from the National Research Council Research Associateship Program at the Naval Research Laboratory. This work was supported by NASA through grant NNX09AD19G. A.C.C. also acknowledges support from the Department of Energy under grant DE-FG02-87ER40317. D.M.T. received support from the Bart J. Bok fellowship at the University of Arizona for part of this work. The authors acknowledge the hospitality of the Kavli Institute for Theoretical Physics, which is supported by the NSF under grant PHY05-51164, during the programs “Accretion and Explosion: the Astrophysics of Degenerate Stars” and “Stellar Death and Supernovae.” The software used in this work was in part developed by the DOE-supported ASC/Alliances Center for Astrophysical Thermonuclear Flashes at the University of Chicago. We thank Nathan Hearn for making his QuickFlash analysis tools publicly available at <http://quickflash.sourceforge.net>. This work utilized resources at the New York Center for Computational Sciences at Stony Brook University/Brookhaven National Laboratory which is supported by the U.S. Department of Energy under Contract No. DE-AC02-98CH10886 and by the State of New York. Some simulations presented in this work were run on the Ranger supercomputer at the Texas Advanced Computing Center as part of the Extreme Science and Engineering Discovery Environment (XSEDE, formally TeraGrid), which is supported by National Science Foundation grant number OCI-1053575. Computations were also performed under the

Department of Energy 2010 INCITE allocation, *Fundamental Research in Type Ia Supernovae*.

REFERENCES

- Abdel-Gayed, R. G., & Bradley, D. 1981, *RSPTA*, 301, 1
- Arnett, D., & Livne, E. 1994a, *ApJ*, 427, 315
- Arnett, D., & Livne, E. 1994b, *ApJ*, 427, 330
- Aspden, A. J., Bell, J. B., Day, M. S., Woosley, S. E., & Zingale, M. 2008, *ApJ*, 689, 1173
- Aspden, A. J., Bell, J. B., & Woosley, S. E. 2010, *ApJ*, 710, 1654
- Aspden, A. J., Bell, J. B., & Woosley, S. E. 2011, *ApJ*, 730, 144
- Aspden, A. J., Day, M. S., & Bell, J. B. 2011, *JFM*, 680, 287
- Badenes, C., Bravo, E., Borkowski, K. J., & Domínguez, I. 2003, *ApJ*, 593, 358
- Blinnikov, S. I., & Khokhlov, A. M. 1986, *SvAL*, 12, 131
- Bloom, J. S., Kasen, D., Shen, K. J., et al. 2012, *ApJL*, 744, L17
- Bravo, E., & García-Senz, D. 2006, *ApJL*, 642, L157
- Brown, P. J., Dawson, K. S., de Pasquale, M., et al. 2012, *ApJ*, 753, 22
- Bychkov, V., & Liberman, M. A. 1995, *A&A*, 302, 727
- Calder, A. C., Fryxell, B., Plewa, T., et al. 2002, *ApJS*, 143, 201
- Calder, A. C., Krueger, B. K., Jackson, A. P., & Townesley, D. M. 2013, *FrPhy*, 8, 168
- Calder, A. C., Townesley, D. M., Seitenzahl, I. R., et al. 2007, *ApJ*, 656, 313
- Chamulak, D. A., Brown, E. F., & Timmes, F. X. 2007, *ApJL*, 655, L93
- Chamulak, D. A., Meakin, C. A., Seitenzahl, I. R., & Truran, J. W. 2012, *ApJ*, 744, 27
- Chandrasekhar, S. 1981, *Hydrodynamic and Hydromagnetic Stability* (New York: Dover)
- Charlette, F., Meneveau, C., & Veynante, D. 2002a, *CoFl*, 131, 159
- Charlette, F., Meneveau, C., & Veynante, D. 2002b, *CoFl*, 131, 181
- Cho, J., Lazarian, A., & Vishniac, E. T. 2003, in *Turbulence and Magnetic Fields in Astrophysics*, ed. E. Falgarone & T. Passot (Lecture Notes in Physics, Vol. 614; Berlin: Springer), 56
- Ciaraldi-Schoolmann, F., Schmidt, W., Niemeyer, J. C., Röpke, F. K., & Hillebrandt, W. 2009, *ApJ*, 696, 1491
- Colella, P., & Glaz, H. M. 1985, *JCoPh*, 59, 264
- Colella, P., & Woodward, P. R. 1984, *JCoPh*, 54, 174
- Colin, O., Ducros, F., Veynante, D., & Poinso, T. 2000, *PhFI*, 12, 1843
- Conley, A., Guy, J., Sullivan, M., et al. 2011, *ApJS*, 192, 1
- Dan, M., Rosswog, S., Guillochon, J., & Ramirez-Ruiz, E. 2011, *ApJ*, 737, 89
- Dan, M., Rosswog, S., Guillochon, J., & Ramirez-Ruiz, E. 2012, *MNRAS*, 422, 2417
- Darrieus, G. 1938, *Propagation d’un front de flamme*, communication presented at La Technique Moderne, Paris
- Davidson, P. A. 2004, *Turbulence: An Introduction for Scientists and Engineers* (Oxford: Oxford Univ. Press)
- Driscoll, J. F. 2008, *PrECS*, 34, 91
- Dursi, L. J., Zingale, M., Calder, A. C., et al. 2003, *ApJ*, 595, 955
- Filippenko, A. V. 1997, *ARA&A*, 35, 309
- Fisher, R. T., Kadanoff, L. P., Lamb, D. Q., et al. 2008, *IBMJ*, 52, 127
- Fryxell, B., Olson, K., Ricker, P., et al. 2000, *ApJS*, 131, 273
- Golombek, I., & Niemeyer, J. C. 2005, *A&A*, 438, 611
- Helmholtz, H. 1868a, *Monatsberichte der Königlichen Preussische Akademie der Wissenschaften zu Berlin*, 23, 215
- Helmholtz, H. 1868b, *Philosophical Magazine Series 4*, 36, 337
- Hillebrandt, W., & Niemeyer, J. C. 2000, *ARA&A*, 38, 191
- Höflich, P., Wheeler, J. C., & Thielemann, F. K. 1998, *ApJ*, 495, 617
- Höflich, P., & Khokhlov, A. 1996, *ApJ*, 457, 500
- Höflich, P., Khokhlov, A. M., & Wheeler, J. C. 1995, *ApJ*, 444, 831
- Iben, I., Jr., & Tutukov, A. V. 1984, *ApJS*, 54, 335
- Jackson, A. P., Calder, A. C., Townesley, D. M., et al. 2010, *ApJ*, 720, 99
- Ji, S., Fisher, R. T., García-Berro, E., et al. 2013, *ApJ*, 773, 136
- Jordan, G. C., IV, Fisher, R. T., Townesley, D. M., et al. 2008, *ApJ*, 681, 1448
- Jordan, G. C., IV, Graziani, C., Fisher, R. T., et al. 2012a, *ApJ*, 759, 53
- Jordan, G. C., IV, Perets, H. B., Fisher, R. T., & van Rossum, D. R. 2012b, *ApJL*, 761, L23
- Kasen, D. 2006, *ApJ*, 649, 939
- Kasen, D., & Woosley, S. E. 2007, *ApJ*, 656, 661
- Kerstein, A. R. 2001, *PhRvE*, 64, 066306
- Khokhlov, A. 1993, *ApJL*, 419, L77
- Khokhlov, A. M. 1991, *A&A*, 245, 114
- Khokhlov, A. M. 1995, *ApJ*, 449, 695
- Khokhlov, A. M. 2000, *astro-ph/0008463*
- Khokhlov, A. M., Oran, E. S., & Wheeler, J. C. 1997, *ApJ*, 478, 678
- Kolmogorov, A. 1941, *DoSSR*, 30, 301
- Kolmogorov, A. N. 1991, *RSPSA*, 434, 9

- Kromer, M., Fink, M., Stanishev, V., et al. 2013, *MNRAS*, **429**, 2287
- Krueger, B. K., Jackson, A. P., Townsley, D. M., et al. 2010, *ApJL*, **719**, L5
- Landau, L. 1944, *Acta Physicochimica*, U.R.S.S., 19, 77
- Landau, L. D., & Lifshitz, E. M. 1987, *Fluid Mechanics* (2nd ed.; Oxford: Pergamon)
- Livne, E. 1990, *ApJL*, **354**, L53
- Markstein, G., for Aeronautical Research, N. A. T. O. A. G., & Development., 1964, *Nonsteady Flame Propagation*, Agardograph Series (Published for and on behalf of Advisory Group for Aeronautical Research and Development, North Atlantic Treaty Organization by Pergamon Press)
- Meneveau, C., & Poinot, T. 1991, *CoFI*, **86**, 311
- Nandkumar, R., & Pethick, C. J. 1984, *MNRAS*, **209**, 511
- Niemeyer, J. C. 1999, *ApJL*, **523**, L57
- Niemeyer, J. C., & Hillebrandt, W. 1995, *ApJ*, **452**, 769
- Niemeyer, J. C., & Kerstein, A. R. 1997, *NewA*, **2**, 239
- Niemeyer, J. C., & Woosley, S. E. 1997, *ApJ*, **475**, 740
- Nomoto, K. 1982a, *ApJ*, **257**, 780
- Nomoto, K. 1982b, *ApJ*, **253**, 798
- Nomoto, K., Thielemann, F.-K., & Yokoi, K. 1984, *ApJ*, **286**, 644
- Nugent, P. E., Sullivan, M., Cenko, S. B., et al. 2011, *Natur*, **480**, 344
- O'Rourke, P. J., & Bracco, F. V. 1979, *JCoPh*, **33**, 185
- Orvedahl, R., Zingale, M., Almgren, A., Bell, J., & Nonaka, A. 2013, in *American Astronomical Society Meeting Abstracts Vol.*, **221**, 240.14
- Pakmor, R., Hachinger, S., Röpke, F. K., & Hillebrandt, W. 2011, *A&A*, **528**, A117
- Pakmor, R., Kromer, M., Röpke, F. K., et al. 2010, *Natur*, **463**, 61
- Pelcé, P. 1988, *Dynamics of Curved Fronts*, Perspectives in Physics (Boston, MA: Academic Press)
- Peters, N. 1988, *Symposium (International) on Combustion*, **21**, 1231
- Peters, N. 2000, *Turbulent Combustion* (Cambridge: Cambridge Univ. Press)
- Phillips, M. M. 1993, *ApJL*, **413**, L105
- Plewa, T., Calder, A. C., & Lamb, D. Q. 2004, *ApJL*, **612**, L37
- Pocheau, A. 1994, *PhRvE*, **49**, 1109
- Poinot, T., & Veynante, D. 2005, *Theoretical and Numerical Combustion* (2nd ed.; Philadelphia, PA: R.T. Edwards)
- Poludnenko, A. Y., & Oran, E. S. 2010, *CoFI*, **157**, 995
- Poludnenko, A. Y., & Oran, E. S. 2011, *CoFI*, **158**, 301
- Raskin, C., Scannapieco, E., Fryer, C., Rockefeller, G., & Timmes, F. X. 2012, *ApJ*, **746**, 62
- Rayleigh. 1882, *Proc. London Mathematical Society*, s1-14, 170
- Reinecke, M., Hillebrandt, W., Niemeyer, J. C., Klein, R., & Gröbl, A. 1999, *A&A*, **347**, 724
- Röpke, F. K. 2006, *RvMA*, **19**, 127
- Röpke, F. K., Hillebrandt, W., & Niemeyer, J. C. 2004, *A&A*, **420**, 411
- Röpke, F. K., Hillebrandt, W., Schmidt, W., et al. 2007, *ApJ*, **668**, 1132
- Röpke, F. K., Niemeyer, J. C., & Hillebrandt, W. 2003, *ApJ*, **588**, 952
- Saio, H., & Nomoto, K. 1985, *A&A*, **150**, L21
- Saio, H., & Nomoto, K. 1998, *ApJ*, **500**, 388
- Saio, H., & Nomoto, K. 2004, *ApJ*, **615**, 444
- Schmidt, W. 2004, PhD thesis, Technical Univ. Munich, Dep. Physics
- Schmidt, W., Niemeyer, J. C., & Hillebrandt, W. 2006a, *A&A*, **450**, 265
- Schmidt, W., Niemeyer, J. C., Hillebrandt, W., & Röpke, F. K. 2006b, *A&A*, **450**, 283
- Schwab, J., Shen, K. J., Quataert, E., Dan, M., & Rosswog, S. 2012, *MNRAS*, **427**, 190
- Seitenzahl, I. R., Ciaraldi-Schoolmann, F., & Röpke, F. K. 2011, *MNRAS*, **414**, 2709
- Seitenzahl, I. R., Meakin, C. A., Lamb, D. Q., & Truran, J. W. 2009, *ApJ*, **700**, 642
- Sytine, I. V., Porter, D. H., Woodward, P. R., Hodson, S. W., & Winkler, K.-H. 2000, *JCoPh*, **158**, 225
- Taylor, G. 1950, *RSPSA*, **201**, 192
- Thomson, W. 1871, *Philosophical Magazine Series 4*, **42**, 362
- Timmes, F. X., & Swesty, F. D. 2000, *ApJS*, **126**, 501
- Timmes, F. X., & Woosley, S. E. 1992, *ApJ*, **396**, 649
- Townsley, D. M., Calder, A. C., Asida, S. M., et al. 2007, *ApJ*, **668**, 1118
- Townsley, D. M., Jackson, A. P., Calder, A. C., et al. 2009, *ApJ*, **701**, 1582
- Vladimirova, N., Weirs, G., & Ryzhik, L. 2006, *CTM*, **10**, 727
- Webbink, R. F. 1984, *ApJ*, **277**, 355
- Whelan, J., & Iben, I., Jr. 1973, *ApJ*, **186**, 1007
- Woosley, S. E. 1990, in *Supernovae*, ed. A. G. Petschek (New York: Springer), **182**
- Woosley, S. E., Almgren, A., Bell, J. B., et al. 2007a, *JPhCS*, **78**, 012081
- Woosley, S. E., Kasen, D., Blinnikov, S., & Sorokina, E. 2007b, *ApJ*, **662**, 487
- Woosley, S. E., Kerstein, A. R., Sankaran, V., Aspden, A. J., & Röpke, F. K. 2009, *ApJ*, **704**, 255
- Yeung, P. K., Girimaji, S. S., & Pope, S. B. 1990, *CoFI*, **79**, 340
- Yoon, S.-C., Podsiadlowski, P., & Rosswog, S. 2007, *MNRAS*, **380**, 933
- Zhang, J., Messer, O. E. B., Khokhlov, A. M., & Plewa, T. 2007, *ApJ*, **656**, 347
- Zingale, M., Almgren, A. S., Bell, J. B., Nonaka, A., & Woosley, S. E. 2009, *ApJ*, **704**, 196
- Zingale, M., & Dursi, L. J. 2007, *ApJ*, **656**, 333
- Zingale, M., Niemeyer, J. C., Timmes, F. X., et al. 2001, in *AIP Conf. Ser. 586, 20th Texas Symposium on Relativistic Astrophysics*, ed. J. C. Wheeler & H. Martel (Melville, NY: AIP), **490**
- Zingale, M., Woosley, S. E., Bell, J. B., Day, M. S., & Rendleman, C. A. 2005a, *JPhCS*, **16**, 405
- Zingale, M., Woosley, S. E., Rendleman, C. A., Day, M. S., & Bell, J. B. 2005b, *ApJ*, **632**, 1021